Two-Dimensional Nonlinear Earthquake Response Analysis of a Bridge-Foundation-Ground System

Yuyi Zhang,[a] Joel P. Conte,[b] Zhaohui Yang,[c] Ahmed Elgamal,[d] Jacobo Bielak,[e] and Gabriel Acero[f]

This paper presents a two-dimensional advanced nonlinear FE model of an actual bridge, the Humboldt Bay Middle Channel (HBMC) Bridge, and its response to seismic input motions. This computational model is developed in the new structural analysis software framework *OpenSees*. The foundation soil is included to incorporate soil-foundation-structure interaction effects. Realistic nonlinear constitutive models for cyclic loading are used for the structural (concrete and reinforcing steel) and soil materials. The materials in the various soil layers are modeled using multi-yield-surface plasticity models incorporating liquefaction effects. Lysmer-type absorbing/transmitting boundaries are employed to avoid spurious wave reflections along the boundaries of the computational soil domain. Both procedures and results of earthquake response analysis are presented. The simulation results indicate that the earthquake response of the bridge is significantly affected by inelastic deformations of the supporting soil medium due to lateral spreading induced by soil liquefaction. [DOI: 10.1193/1.2923925]

INTRODUCTION

Earthquake-resistant design of a structural system requires analysis to predict its deformations and internal forces due to potential earthquakes. A wide range of seismic structural analysis methods (from simple to sophisticated ones) is available. The level of sophistication required depends on the purpose of the analysis in the design process. However, an appropriate model of the structure and realistic representation of the earthquake ground motion are essential in all methods. The model should represent with sufficient fidelity the spatial distribution and/or possible evolution of the stiffness, strength, deformation capacity, and mass of the structure. Nonlinear relations between forces and deformations/displacements due to material and/or geometric nonlinearities are now widely used in structural analysis. The structural response history due to an earthquake can be computed through dynamic analysis. This paper presents an advanced nonlinear

[a] Research Scientist, ANATECH Corp., 5435 Oberlin Dr., San Diego, CA 92121
[b] Prof., Dept. of Structural Eng., Univ. of California, San Diego, La Jolla, CA 92093-0085
[c] Engineer, URS Corporation, 1333 Broadway, Suite 800, Oakland, CA 94612
[d] Prof., Dept. of Structural Eng., Univ. of California, San Diego, La Jolla, CA 92093-0085
[e] Prof., Dept. of Civil and Env. Eng., Carnegie-Mellon Univ., Pittsburgh, PA 15213
[f] Design Engineer, Myers, Houghton & Partners, 4500 E. Pacific Coast Hwy., Ste. 100, Long Beach, CA 90804

time history analysis of a bridge-foundation-ground (BFG) system subjected to seismic excitation. The modeling and analysis method used can be readily applied to other types of structures.

A number of researchers have recently investigated through analytical studies the seismic behavior of bridges including the effects of soil-structure interaction (SSI). Some of them used motions of bridges recorded during actual earthquake events and performed system identification studies to estimate the actual vibration properties of the bridge systems and to elucidate the effects of the abutments, approach embankments (ramps), and soil-foundation-structure interaction on the seismic response of these bridges. It was found that for short-span overpass bridges, the bridge superstructure, abutments and approach embankment soil behave as an integrated system during earthquakes. Furthermore, the dynamic behavior of the foundation soil and embankment soil were found to have significant influence on the seismic response of the bridge superstructure (Werner et al. 1987, 1990, and 1994; Wilson and Tan 1990a and 1990b). Goel (1997) and Goel and Chopra (1997) identified the vibration properties of a two-span concrete bridge with integral abutments from its response recorded during real earthquake events to study the effects of the abutments on the seismic behavior of this bridge. Their results indicate that abutment participation as well as nonlinear soil behavior and SSI plays a significant role in the seismic response of the bridge.

Dynamic analysis is used increasingly to assess the safety of existing bridges in locations of high seismic risk and to develop appropriate retrofit strategies. In particular, Dendrou et al. (1985) developed a methodology to analyze the effects of traveling seismic waves on the dynamic response of an elastic concrete bridge. In their analysis, the bridge system is represented using a three-dimensional finite element (FE) model, while the underlying soil medium is modeled using a boundary integral method. A substructuring approach is used to model the bridge-soil dynamic interaction. Seismic excitations are induced by plane shear and Rayleigh waves and their effects on the concrete deck are evaluated in terms of various displacement response quantities. Mylonakis et al. (1997) also implemented a sub-structuring method for the seismic analysis of bridge piers founded on vertical piles and pile groups in multi-layered soil. For typical bridge piers founded on soft soil, they explore the importance of soil-pile-bridge interaction through a parameter study.

In other studies (Spyrakos 1992; Ciampoli and Pinto 1995; Mylonakis and Gazetas 2000; Zhang and Makris 2002; Kappos et al. 2002; Jeremic et al. 2004), a detailed model of the bridge structure (aboveground) is developed including material nonlinearities, with the foundation soil replaced by equivalent springs and dampers, and dynamic analyses of the structure, spring and damper system are performed. This approach partially accounts for soil-foundation-structure interaction effects at minimum additional computational cost. However, in reality the dynamic behavior (both linear and nonlinear) of the foundation soil is too complicated to be simplified into springs and dampers with constant parameters. In addition, due to SSI effects, the earthquake ground motion along the soil-structure interface differs from the free-field motion, which is commonly used in these studies as input seismic excitation applied at the fixed-end of the springs and dampers. Surface ground motions at different locations at any given instant are generally

different in both amplitude and phase due to the propagating nature of seismic waves. This effect is very important for bridges, which generally have spatially extended foundations. Thus, it is important to represent the foundation soil explicitly in an analytical bridge model in order to fully capture the SSI mechanism (Clough and Penzien 2003). In a comprehensive study, McCallen and Romstadt (1994) developed a detailed nonlinear (material) three-dimensional FE model of an actual soil-foundation-bridge system, modeling explicitly the soil and pile group foundations. Using this model, they performed an eigenvalue analysis (at the initial stiffness properties) and nonlinear seismic response history analyses, obtained some enlightening results such as the significant effects of the stiffness and inertia of the soil embankments on the natural vibration properties and seismic behavior of the overall system, and calibrated the high-level modal damping to be used in an equivalent linear elastic stick model of the bridge (as typically used in engineering practice). The model used to determine the system natural vibration properties extends vertically to a depth corresponding to the nominal pile tip elevation. However, in their seismic response calculations, they truncated the detailed model at approximately the original grade elevation (i.e., only the bridge structure above ground surface and the soil embankment were retained) and utilized the free field ground motion directly as uniform input at the fixed base of the truncated model. A simple Ramberg-Osgood elastoplastic model was fitted to the standard shear modulus reduction and damping curves developed by Seed et al. (1984) to represent the nonlinear hysteretic behavior of the soil embankments.

This paper focuses on the Humboldt Bay Middle Channel (HBMC) Bridge near Eureka in northern California, which was selected as a bridge testbed by the Pacific Earthquake Engineering Research (PEER) Center in order to apply and evaluate the PEER performance-based earthquake engineering (PBEE) methodology (Porter 2003). A two-dimensional, advanced nonlinear FE model of this bridge system including the structure, pile group foundations, approach embankments and foundation soil is developed in *OpenSees* (McKenna and Fenves 2001), the new software framework for advanced nonlinear modeling and analysis of structural and/or geotechnical systems developed by PEER. In the present model, the foundation soil is modeled explicitly as a multi-layered elastoplastic continuum, with incorporation of liquefaction effects. This model is also the basis from which large ensembles of nonlinear response history analyses are to be performed to predict the seismic demand of the bridge system in probabilistic terms as one of the analytical steps of the PEER PBEE methodology. Thus, in order to benefit from a FE model that is numerically robust to the implicit integration of the equations of motion for ensembles of seismic inputs, as well as to achieve an acceptable computational time (not exceeding 18 hours per response history analysis on a regular PC), a two-dimensional, instead of three-dimensional, model of the bridge system is developed herein. This provides a first step towards a more realistic three-dimensional representation of the earthquake response behavior of the bridge system. This paper focuses only on the longitudinal response of the bridge system assuming plane strain condition for the soil domain, which does not imply that the transversal response of the bridge is insignificant or irrelevant and should be ignored. Realistic nonlinear inelastic constitutive models are used for the structural (concrete and reinforcing steel) and soil materials under cyclic loading. Lysmer-type transmitting/absorbing boundaries are implemented in
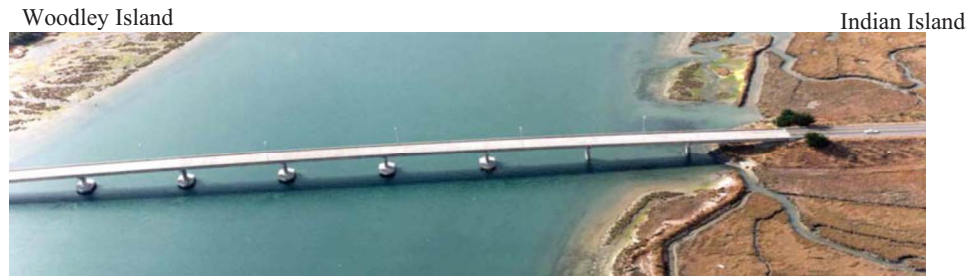
Woodley Island   Indian Island

Figure 1. Aerial view of Humboldt Bay Middle Channel Bridge (courtesy of California Department of Transportation (Caltrans)).

this model and special measures are taken to define the seismic input at the base of the computational soil domain. For each response history analysis, a staged analysis procedure is adopted in which the gravity forces of the soil (first) and bridge (second) are applied quasi-statically followed by the dynamic application of the seismic excitation. Representative responses of the model to an occasional earthquake (with a probability of exceedance of 50% in 50 years, return period of 72.5 years) and a very rare earthquake (with a probability of exceedance of 2% in 50 years, return period of 2,475 years) are presented and discussed.

HUMBOLDT BAY MIDDLE CHANNEL BRIDGE

DESCRIPTION OF STRUCTURE

The Humboldt Bay Bridge site, located near Eureka in northern California, includes three bridges, Eureka Channel Bridge, Middle Channel Bridge and Samoa Channel Bridge, over waterways crossing Woodley Island and Indian Island. The Middle Channel Bridge (Figure 1) is 330-meter long, 10-meter wide, and 12-meter high (average height over mean water level). The nine span superstructure consists of four precast prestressed concrete I-girders and cast-in-place concrete slabs, as shown in Figure 2. The bridge superstructure is supported by two seat-type abutments and eight bents founded on pile group foundations, each bent consisting of a single column and hammer head cap beam. The height of the columns/piers ranges from 11 m to 14 m. The deep foundations consist of driven precast prestressed concrete pile groups supporting pile caps. Each abutment is supported on two rows of piles, with 7 front batter square piles (356 mm/14 in side), and 5 rear vertical square piles (356 mm/14 in), of 400 kN capacity per pile. For convenience, the piers are numbered #1 through 8 from the left (South-East, Woodley Island side) to the right (North-West, Indian Island side). Piers #2 through 6 are supported on five 1372 mm (54 in) diameter, 1800 kN circular piles, while piers #1, 7 and 8 are supported on sixteen (4 rows of 4 piles) 356 mm (14 in), 625 kN square piles. All piers and piles have continuous moment connection at the pile-cap-pier joints. The superstructure is continuous over piers #1, 2, 4, 5, 7 and 8. There are expansion joints at the abutments and on top of piers #3 and 6. At these expansion joints, there are shear

Figure 2. Superstructure of Humboldt Bay Middle Channel Bridge.

keys with gaps on both sides; while at the continuous joints, a shear key with #4 dowels connects the superstructure to the cap beam of the single column bent (i.e., shear key without gap). Thus, the bridge structure consists of three frames interconnected through shear keys with gaps at the two interior expansion joints.

DESCRIPTION OF SITE CONDITIONS

Ten rotary auger borings were drilled to a maximum depth of about 30 m below the existing ground surface in 1967. These borings were almost evenly distributed between the two abutments along the centerline of the bridge. Another rotary auger boring to a depth of about 64 m below the existing ground surface was drilled near the second span of the bridge from the Eureka side by the Caltrans' Office of Structural Foundations in 1994. Based on these data (Caltrans 2000), a generalized soil profile was developed. The bridge alignment, to the maximum explored depth, is underlain by Tertiary and Quaternary Alluvial deposits (soil layer 1 in Figure 3). A 1.5 to 3.0 m thick surficial soil layer consisting of mainly soft to very soft organic silt with clay and some construction debris blankets the entire bridge alignment (soil layer 8 in Figure 3). This surficial layer from near the left abutment to near pier #2 is underlain by about 10.8 m of medium dense to dense silty sand and sand with some organic matter (soil layer 5 in Figure 3). The surficial layer from the vicinity of pier #7 to the vicinity of the right abutment is underlain by a layer of soft or loose sandy silt or silty sand with organic matter (soil layer 7 in Figure 3). The thickness of this layer varies significantly and ranges from about 1.5 m near pier #7 to over 15 m near the right abutment. The surficial layer along the remainder of the
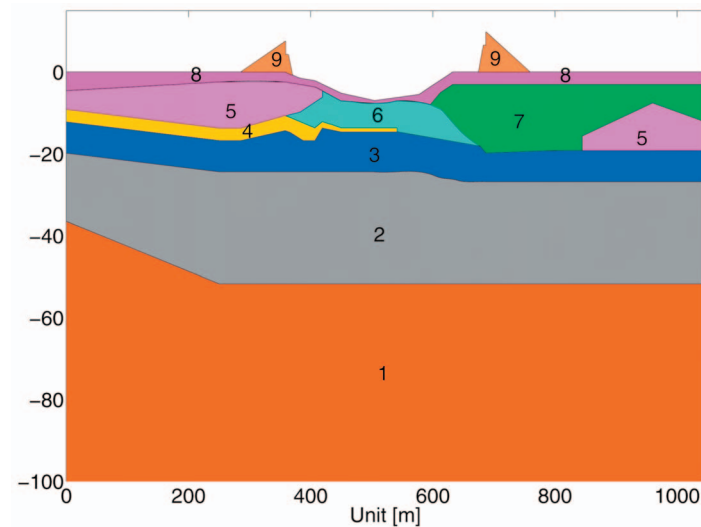
Figure 3. Two-dimensional soil profile of HBMC Bridge site (layer 1: Tertiary and Quaternary Alluvial deposits; layer 2: medium dense organic silt, sandy silt and stiff silty clay; layer 3: dense sand; layer 4: silt; layer 5: medium dense to dense silty sand and sand with some organic matter; layer 6: dense silty sand and sand; layer 7: soft or loose sandy silt or silty sand with organic matter; layer 8: soft to very soft organic silt with clay; and layer 9: abutment fill. Layers 5 and 7 are susceptible to soil liquefaction.

bridge alignment in the middle of the river channel is underlain by about 9.2 m of mainly dense silty sand and sand (soil layer 6 in Figure 3). A 7.6 to 10.7 m thick layer of mainly very dense sand underlies the above soil layers along the entire bridge alignment (soil layer 3 in Figure 3). This very dense sand layer is underlain, to the maximum explored depth (64 m), by mainly medium dense organic silt, sandy silt and stiff silty clay (soil layer 2 in Figure 3). Groundwater was encountered at ground surface in the land borings drilled in 1967. Recent field observations also showed that the water in the channel is near the ground surface level.

Borehole 1 at Caltrans Samoa Bridge geotechnical downhole array (approximately 0.25 mile north-west of the west abutment of the HBMC Bridge) provides a shear wave velocity profile down to a depth of 220 meters (see Figure 4), where the borehole encountered bedrock (shear wave velocity >850 m/sec). The shear wave velocities are about 180 m/sec in the upper 20 m, lie in the range of 200 to 400 m/sec in the depth range of 20 to 60 m, and lie in the range of 400 to 600 m/sec in the depth range of 60 to 220 m (Somerville and Collins 2002). The Humboldt Bay bridge site is susceptible to soil liquefaction under strong ground shaking. Soil liquefaction, approach fill settlement and lateral spreading are issues of interest in this study.
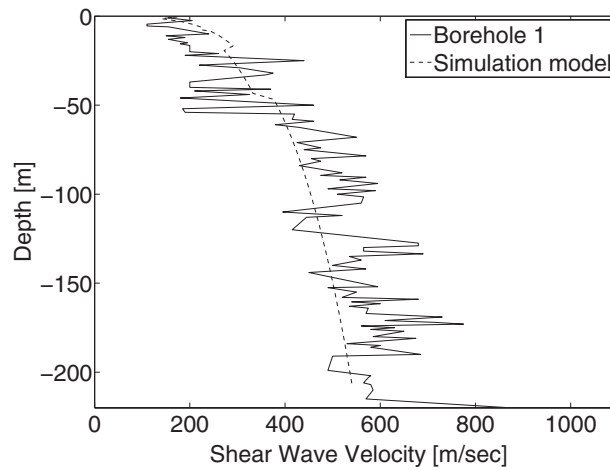
Figure 4. Shear wave velocity profile near HBMC Bridge site.

FAULTING AND SEISMICITY

The Humboldt Bay bridges are located in an area of complex tectonic interaction among the Gorda, North American and Pacific Plates. The "Little Salmon" fault, which is categorized by the California Department of Mines and Geology as one of the principal active fault in California, is the nearest seismic source from the site. This fault is located about 5 km from the Humboldt Bay Bridges and is capable of generating a Maximum Credible Earthquake of Moment Magnitude 7.5. According to the site-specific seismic ground motion study conducted by Geomatrix Consultants (1994) for Caltrans, the Peak Bedrock Acceleration at the bridge location was estimated to about 0.9 g.

SEISMIC RETROFITS

The HBMC Bridge was designed in 1968 and built in 1971 and has been the object of two Caltrans seismic retrofit efforts, the first one completed in 1995, and the second one completed in 2005. The objectives of the first retrofit effort were to mitigate the potential for unseating and diaphragm damage and to strengthen the shear keys by enlarging and reinforcing the superstructure. In this retrofit, the transverse end diaphragms on top of all piers (at both expansion and continuous joints) were replaced by stronger ones; cable restrainers and pipe seat extenders were installed at the expansion joints to connect adjacent superstructures; seat width at the abutments and interior expansion joints was increased; and shear keys at all joints were strengthened. The objective of the second retrofit was to strengthen the substructure (piers, pile caps, and pile groups) and consisted of (Caltrans 2002): (1) placing reinforced concrete casings around each pier; (2) increasing the horizontal size of the pile cap and adding four 900 mm (36 in) diameter cast-in-steel shell piles at each pier; and (3) adding a 450 mm (18 in) thick reinforced concrete top mat to the pile cap of each pier.
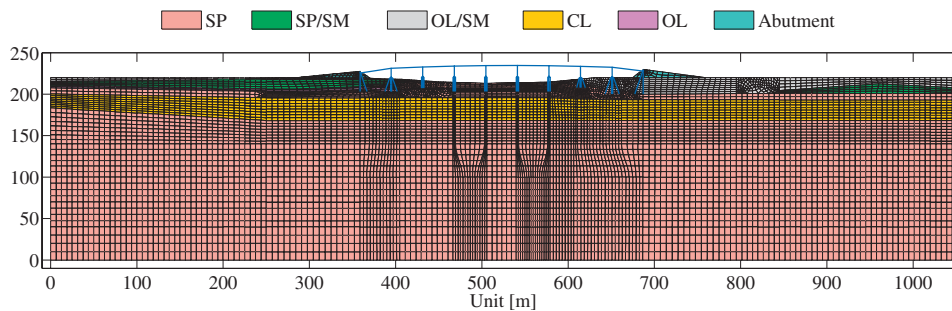
Figure 5. OpenSees finite element model of HBMC bridge-foundation-ground system [based on blue prints courtesy of Caltrans, mesh constructed using GID, a graphical pre- and post-processor for computer simulation (Dominguez and Soler 1999)].

COMPUTATIONAL MODEL

A two-dimensional nonlinear finite element model (shown in Figure 5) of the HBMC Bridge in its "as-built" condition, including the superstructure, piers, pile group foundations, abutments, embankment approaches, and foundation soil, was developed in the software framework OpenSees. This model includes 10,889 nodes, 10,600 elements and 20,686 degrees of freedom. As already mentioned, this study investigates the seismic response behavior of the bridge in the longitudinal direction only.

FOUNDATION SOIL

Although the seismic response of the BFG system considered is inherently a 3-D problem, in a first analysis step, a 2-D representation of the foundation soil was used by assuming plane strain condition. For a more complete and quantitatively more accurate analysis, a 3-D model of the BFG system is clearly needed. Previous researchers (Luco and Hadjian 1974) have studied the feasibility of representing a 3-D linear soil-structure interaction problem by a 2-D plane strain model. They concluded that by properly selecting the 2-D model, it was possible to obtain close approximations to the system frequencies, but that the damping (radiation damping) associated with the low-frequency modes is significantly over-estimated. In spite of the clear limitations of the 2-D model of the BFG system considered here, it is believed that it is able to capture (at least qualitatively) the key aspects of the effects of soil lateral spreading on the overall seismic response mechanism of the BFG system. The dimensions of the soil domain considered in the 2-D model of the BFG system are 1,050 m in length and 220 m in depth (bedrock level). The soil domain is taken sufficiently long so as to satisfy the following criteria for the soil response away from its lateral boundaries: (1) the simulated soil response assuming homogeneous, linear elastic, undamped soil material in the entire computational soil domain, is sufficiently close to that of a shear soil column made of the same material; and (2) the vertical component of the simulated nonlinear soil response remains relatively small compared to the horizontal component at the same location. The soil domain is spatially discretized using four-noded, bilinear, isoparametric finite elements

with four integration points each. The size of the finite elements throughout the soil domain is controlled by the soil shear wave velocity profile (see Figure 4) such that shear waves up to about 15 Hz can be propagated with sufficient accuracy through the soil mesh. The (out of plane) thickness of the soil domain below the water table (i.e., ground surface) is taken as 6.10 m, which corresponds to the width of the 1372 mm (54 in.) pile groups supporting the bridge piers, while a thickness of 10.4 m, equal to the separation distance between the abutment wing walls, is used for the approach embankments. The selection of the out-of-plane thickness of the foundation soil was based on the consideration of two opposing effects: (1) piles near the longitudinal axis of the bridge deform more, longitudinally, than the piles further away (i.e., the effective width of a pile group is smaller than its actual width), and (2) soil outside the (out-of-plane) width of the foundation groups also contributes to the seismic response of the BFG system (i.e., contributes to added/entrained mass of soil) in the longitudinal direction.

According to the idealized soil profile developed above (see Figure 3), the soil domain is divided into the following layers as shown in Figure 5 (from bedrock to ground surface): (1) dense to very dense, fine to medium grained sand (SP), (2) organic silt (OL), (3) dense to very dense, fine to medium grained sand (SP), (4) very stiff clay (CL), (5) medium dense, silty sand (SP/SM), (6) dense sand (SP), (7) loose sandy silt, silty sand with organic matter (OL/SM), (8) soft organic silt (OL), and (9) abutment fill, compact medium dense sand.

The abutment fill is modeled as dry material, while the other soil layers, which are below the water table, are modeled as saturated materials with simplified treatment of liquefaction effects based on the assumption of undrained conditions. Two types of soil material constitutive models are used in this study: pressure independent and pressure dependent material models. These models are formulated in effective stress space and are based on multi-yield-surface (i.e., nested yield surfaces) plasticity. The pressure independent model is an elastoplastic model for simulating monotonic and cyclic response of materials whose shear behavior is insensitive to changes in the confining pressure. In this model, a set of Von Mises yield surfaces with different sizes form the hardening zone as shown in Figure 6. The outermost surface defines the shear strength (or failure) envelope. Nonlinear kinematic hardening and associative flow rules (Prevost 1985) are employed to reproduce Masing-type hysteretic behavior. The pressure dependent model is an elastoplastic model for simulating the monotonic and cyclic key response characteristics of soil materials with mechanical (properties) behavior that depends on the confining pressure. Such characteristics include dilatancy (shear-induced volume contraction or dilation) and non-flow liquefaction (cyclic mobility), typically exhibited in medium to dense sands or silts during monotonic and cyclic loading. In this model, a set of Drucker-Prager nested yield surfaces with a common apex and different sizes form the hardening zone as shown in Figure 7. The outermost surface defines the shear strength (or failure) envelope. Nonlinear kinematic hardening and non-associative flow rules are employed to reproduce the dilatancy effect (Elgamal et al. 2003). These soil models have been extensively calibrated and validated for both drained (dry) and
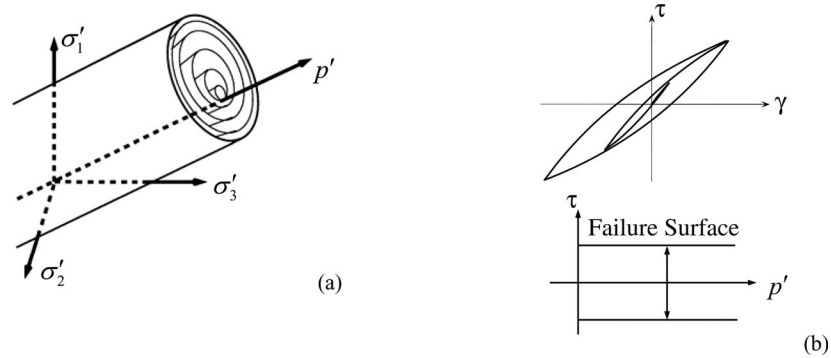
Figure 6. Pressure independent soil material model: (a) yield surface configuration in principal effective stress space, and (b) illustration of constitutive model response.

undrained (liquefaction) conditions based on various laboratory tests (e.g., Arulmoli et al. 1992; Kammerer et al. 2000), centrifuge experiments (e.g., Dobry et al. 1995), and downhole-array seismic records (e.g., Elgamal et al. 2001).

Pressure independent material constitutive laws are employed to model the solid phase of clay and silt (soil layers 2, 4, 7, 8, and 9 in Figure 3), while pressure dependent material constitutive laws are used to model the solid phase of sand and silty sand (soil layers 1, 3, 5, and 6 in Figure 3). In order to simulate undrained response in saturated soil layers, the above material models of solid phase are embedded in a linear elastic material model with high bulk modulus (i.e., nearly incompressible) to model the fluid phase (Yang et al. 2005). Material constitutive parameters were determined for the various soil layers based on SPT (i.e., $(N_1)_{60}$) data and laboratory sample test results (undrained shear strength, unit weight) provided by Caltrans as well as various empirical relations (Meyerhof 1956; Mitchell and Katti 1981; Duncan et al. 1989). The most
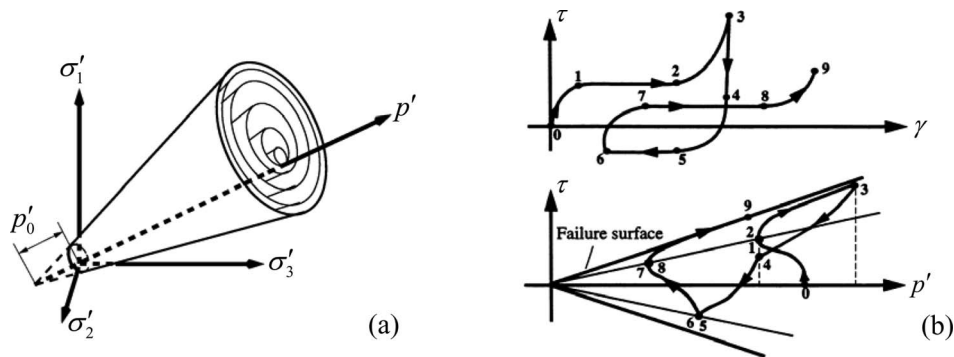

Figure 7. Pressure dependent soil material model: (a) yield surface configuration in principal effective stress space, and (b) schematic of constitutive model response.

Table 1. Primary material parameters of foundation soil layers

Soil layer	Average $(N_1)_{60}$[a]	Saturated unit weight (ton/m^3)	G_{max}[b] (kPa)	Friction angle (degrees)	Cohesion (kPa)
1, 3 and 6 (SP)	50	2.1	5.3×10^5	42	0
2 (OL)	14	2.0	4.8×10^5	35	70
4 (CL)	20	1.8	4.0×10^5	0	100
5 (SP/SM)	20	1.9	2.4×10^5	35	0
7 and 8 (OL/SM)	7	1.9	2.4×10^5	0	35
9 (abutment fill)	—	1.9	1.0×10^5	30	30

[a] standard penetration resistance, corrected for the energy of the hammer and to an overburden pressure of 100 kPa
[b] at 80 kPa mean effective confinement

significant material parameters including the friction angle, cohesion, and initial (low strain) shear modulus are reported in Table 1. In the case of clay and silt materials, these primary soil parameters are sufficient to characterize completely the pressure independent soil models (Yang et al. 2003). For pressure dependent soil materials, in addition to these primary parameters, other parameters governing the dilatancy behavior were calibrated based on the simplified procedure for liquefaction susceptibility (Youd et al. 2001) and using empirical relations proposed by Seed et al. (2003) and Liu et al. (2001).

The soil shear wave velocity profile measured at the Caltrans' Samoa Bridge Geotechnical downhole array (Borehole 1) is shown in Figure 4 where it is also compared to its counterpart from the computational soil model. The latter also accounts for the increase of the low-strain shear modulus with depth within the same soil layer due to increase in confining pressure.

STRUCTURE

Abutments

The abutment seats are modeled using quadrilateral plane-strain elements made of isotropic linear elastic material and embedded in the soil mesh. The back wall is modeled using linear elastic beam-column elements. Young's modulus and Poisson's ratio of the abutments and back wall are taken as that of concrete (E_c=28 GPa and v_c=0.20).

Girders

Because of the high axial stiffness of the superstructure composed of four prestressed, precast I-girders and the slab, the deformation of the superstructure in the longitudinal direction of the bridge (between two expansion joints) is negligible compared to the longitudinal deformation (drift) of the bridge piers. Also, the strength (flexural and shear) of the superstructure is higher than that of the bridge piers lap-spliced at the base. Therefore, it is reasonable to model the superstructure with equivalent linear elastic
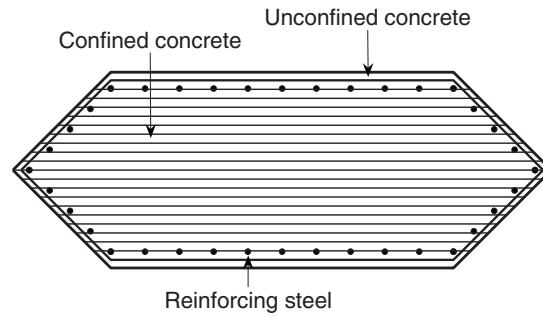
Figure 8. Fiber discretization of piers cross section.

beam-column elements (one per span). The cross sectional area (A) of this equivalent beam element is 3.45 m^2, while its moment of inertia is 1.68 m^4. Young's modulus of the superstructure is also taken as that of concrete (E_c=28 GPa).

Lap Spliced Piers

Each bridge pier is modeled via a single fiber-section beam-column element with five Gauss-Lobatto (G-L) points along its length. This element is formulated using the flexibility (or force-based) approach based on the exact interpolation of the internal forces (Spacone et al. 1996). The cross sections at the five G-L points are discretized into fibers of confined concrete (core), unconfined concrete (cover) and reinforcing steel as shown in Figure 8. The uniaxial Kent-Scott-Park constitutive model (Figure 9) with degraded linear unloading/reloading stiffness and no tensile strength is employed to model the concrete material (Kent and Park 1971). The loading branch of this model is described by a parabolic function as
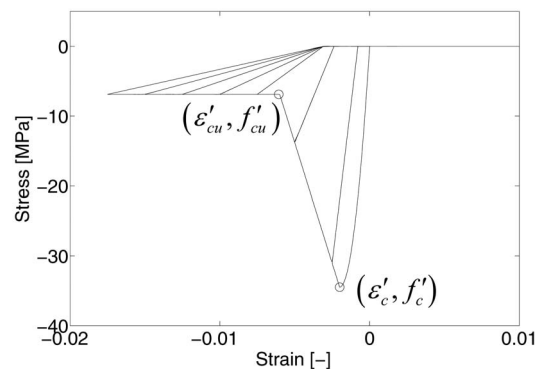
Figure 9. Uniaxial cyclic Kent-Park-Scott concrete model.

Table 2. Material parameters for concrete in bridge piers, pile foundations and pile caps

Component	Concrete material	Compressive strength f'_c (kPa)	Strain at compressive strength, ε'_c	Crushing strength f'_{cu} (kPa)	Strain at crushing strength, ε'_{cu}
Piers	Confined	−34485 (−5.00 ksi)	−0.002	−6897 (−1.00 ksi)	−0.006
	Unconfined	−27588 (−4.00 ksi)	−0.002	0.0	−0.005
356 mm	Confined	−57039 (−8.27 ksi)	−0.005	−43728 (−6.34 ksi)	−0.019
piles	Unconfined	−41383 (−6.00 ksi)	−0.002	−13794 (−2.00 ksi)	−0.006
1372 mm	Confined	−41383 (−6.00 ksi)	−0.004	−27588 (−4.00 ksi)	−0.014
piles	Unconfined	−27588 (−4.00 ksi)	−0.002	0.0	−0.008
Pile caps	Unconfined	−34486 (−5.00 ksi)	−0.004	0.0	−0.006

$$f_c = f'_c \left[\frac{2\varepsilon}{\varepsilon'_c} - \left(\frac{\varepsilon}{\varepsilon'_c} \right)^2 \right] \quad \text{when } \varepsilon \leqslant \varepsilon'_c \tag{1}$$

where f_c, ε, f'_c and ε'_c denote the stress, the corresponding strain, the compressive strength and the strain at peak strength, respectively. Softening beyond the compressive strength is approximated as a linear function. A residual strength (or crushing strength), f'_{cu}, and the corresponding strain ε'_{cu} (strain at crushing strength) are also specified. The parameters of the confined and unconfined concrete materials in the piers are given in Table 2. For the cross sections at the upper four G-L points of each pier element, the uniaxial bilinear material model (or uniaxial J_2 plasticity model with linear kinematic hardening) is used to model the reinforcing steel with the following material parameters: Young's modulus E_s=200 GPa (29000 ksi), yield strength f_y=276 MPa (40 ksi) and post-yield hardening ratio b=0.8%. Figure 10 shows the cyclic moment-curvature response of the pier fiber-section defined at the upper four G-L points of each pier element. At the base of the eight piers, all the longitudinal reinforcing bars are lap spliced. The uniaxial tri-linear hysteretic material model shown in Figure 11 is used to model the reinforcing steel in the lap spliced region. The compression branch is the same as that of the reinforcement steel model used at the upper four G-L points. Points A, B and C on the tension branch correspond to the yield strength, the peak capacity and the residual strength, respectively, of this hysteretic material model. The material properties for this hysteretic material model, given in Table 3, were calibrated based on the envelope (skeleton curve) of the lateral force-deformation (drift) response of the bridge piers as predicted using a detailed mechanics-based model of lap spliced columns (Acero 2005), which accounts for (1) the force transfer mechanism between spliced rebars, (2) the bond-slip degradation, (3) the length of the yield plateau in the stress-strain law of the spliced reinforcing steel, (4) the length of the spliced region, (5) the strain penetration of the longitudinal reinforcement into the foundation, and (6) the axial load ratio. This mechanics-based model was itself calibrated using experimental data on lap-spliced columns. The pier lateral drift (also called tangential drift) is defined herein as the relative top-to-bottom horizontal displacement of the pier, minus the horizontal displacement at the top of the pier due to a rigid body rotation of the pier equal to the rotation of its base.
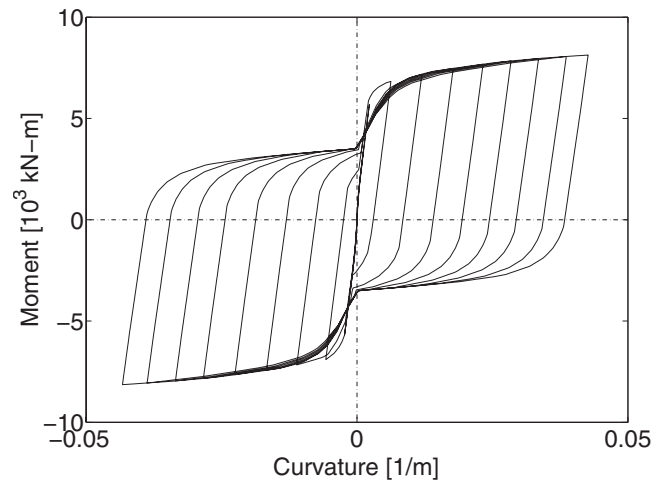
Figure 10. Cyclic moment-curvature response of fiber-section at four upper G-L points of pier elements.

Figure 12 shows the cyclic hysteretic base moment-curvature response of a cantilever pier (of average height) of the HBMC Bridge subjected to quasi-static cyclic loading (with a concentrated horizontal load at the top) of increasing amplitude under constant axial load (corresponding to gravity load condition) as predicted by the computational model of the pier using the calibrated model of the spliced reinforcing steel in the base section (G-L point). A quasi-static monotonic pushover analysis was performed for a single cantilever pier. Figure 13 displays the moment-curvature response at the four
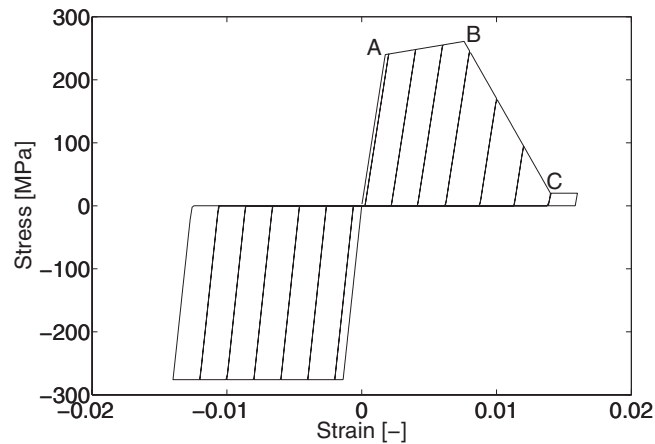
Figure 11. Uniaxial hysteretic model for reinforcing steel at the base cross section of the bridge piers.

Table 3. Parameters of the hysteretic material model used for the tensile branch of the spliced reinforcing steel

	Stress (MPa)	Strain
A	240	0.00175
B	261	0.00760
C	20	0.0140

lower G-L points (the top G-L point corresponding to the free end). As can be seen, the plastic deformations concentrate at the base G-L point (representing the lap spliced region), while the other G-L points undergo quasi-elastic loading and elastic unloading.

Pile Group Foundations and Pile Caps

The HBMC Bridge is supported by two types of pile groups, namely four by four 356 mm (14 in.) square piles and five 1372 mm (54 in.) circular piles (see Figure 14). As a first approximation, each out-of-plane row of piles is lumped into a single equivalent pile with a monolithic cross section defined by the union of the cross sections of the piles in that row and following Bernoulli-Euler beam theory. Each lumped pile is then discretized into a number of force-based, fiber-section beam-column elements (with five G-L points each) to match the FE mesh of the surrounding soil. Each lumped pile cross section is also discretized into fibers of confined and unconfined concrete, and reinforcing steel as shown in Figure 14. The uniaxial Kent-Scott-Park constitutive model and uniaxial bilinear model are used to model the concrete and reinforcing steel, respectively. The pre-stressing effects were incorporated indirectly by calibrating the material parameters so as to match section analysis results obtained by including explicitly the
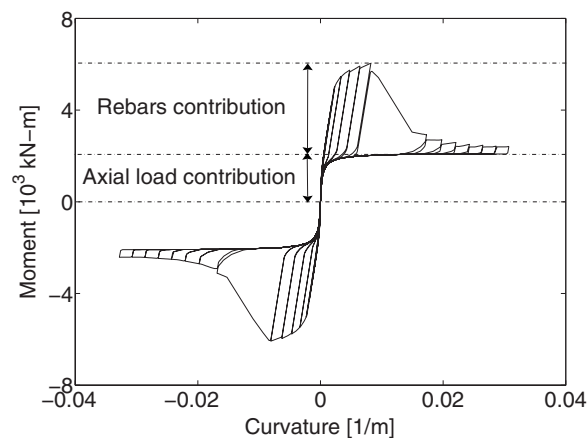
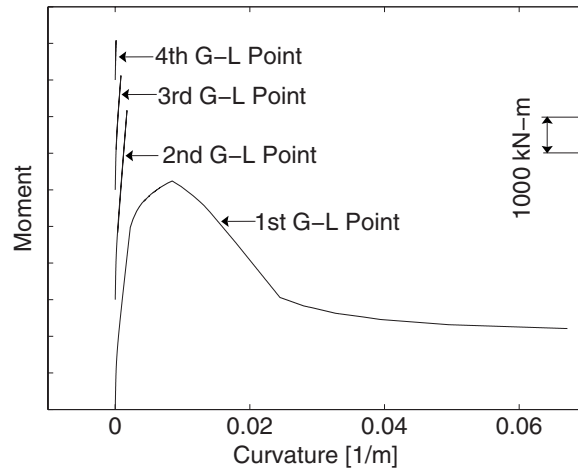**Figure 12.** Simulated cyclic base moment-curvature response of lap-spliced pier.

Figure 13. Moment-curvature responses at four lower G-L points of cantilever bridge pier subjected to quasi-static monotonic pushover (G-L points numbered from bottom to top of pier).

pre-stressing effects (Silva and Seible 2001). These material parameters are given in Tables 2 and 4. The pile nodes are directly connected to the surrounding soil nodes in the translational degrees of freedom. Although pile elements and soil elements have identical translational displacements at the common nodes, their deformed shapes between two consecutive pile nodes are incompatible. As a result, some numerical gap and interpenetration develop along the pile-soil interface. However, this error is considered insignificant in light of the numerous simplifying modeling assumptions made herein. The effects of slippage and friction between soil and piles and/or pile-soil separation (gap-
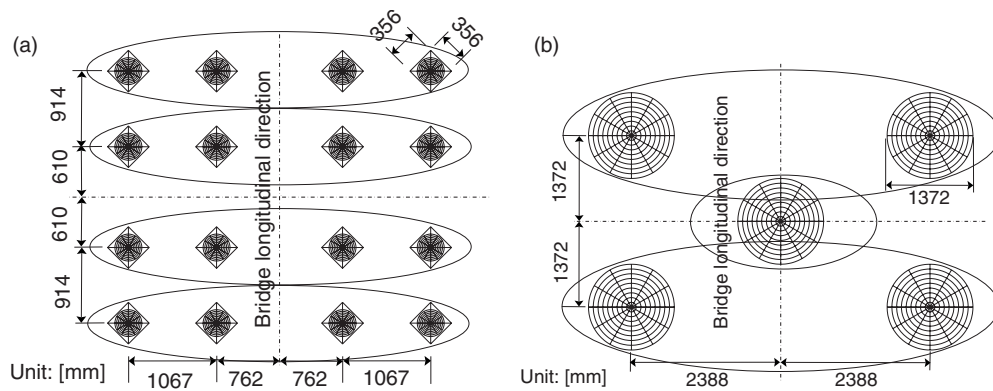
Figure 14. Fiber discretization of the pile group cross sections (the piles in the same ellipse are lumped into a single equivalent pile): (a) 4 by 4 356 mm pile group foundation, and (b) 1372 mm pile group foundation.

Table 4. Material parameters of reinforcing steel in pile foundations and pile caps

Component	Yield strength f_y (MPa)	Young's modulus E_s (GPa)	Hardening ratio, b
356 mm piles	413.8 (60 ksi)	200 (29000 ksi)	0.008
1372 mm piles	413.8 (60 ksi)	200 (29000 ksi)	0.008
Pile caps	413.8 (60 ksi)	200 (29000 ksi)	0.008

ping) near the ground surface are not accounted for in this study, as these effects would require the use of special-purpose pile-soil interface elements. These effects have been studied by other researchers (Trochanis et al. 1991) who found that pile-soil slippage and separation reduce the level of interaction between piles under pure axial loading and pure lateral loading, respectively.

Pile caps are also modeled using force-based, fiber-section beam-column elements with five G-L points along their length. Again, the uniaxial Kent-Scott-Park constitutive model and the uniaxial bilinear model are used for the concrete and reinforcing steel, respectively. The corresponding material parameters are given in Tables 2 and 4.

Shear Keys at Expansion and Continuous Joints

At the abutment (expansion) joints, interior expansion joints and continuous joints, the superstructure is connected to the abutments and piers through shear keys in the longitudinal direction. Figures 15–17 illustrate the FE modeling of these three types of joints. At each joint, an equal degree of freedom constraint in the vertical direction is imposed on each pair of superstructure and abutment/pier-top nodes. The shear keys are modeled using zero-length elements with an aggregated uniaxial material model composed of an "elastoplastic material model with gap," an "elastoplastic material model with hook" and another elastoplastic material model, all configured in parallel. The purpose of the last elastoplastic material model is to represent the friction between the superstructure and the bridge pier. For this model, the yield strain is set at a very small value and the yield strength is set at the friction force. In order to simulate the physical fracture of these shear keys, an ultimate deformation is specified for each shear key aggregated material model so that its internal force drops to zero when this deformation is reached and remains zero thereafter. The material properties of the uniaxial material
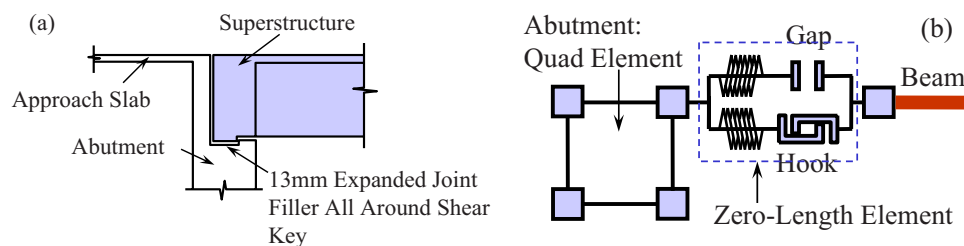
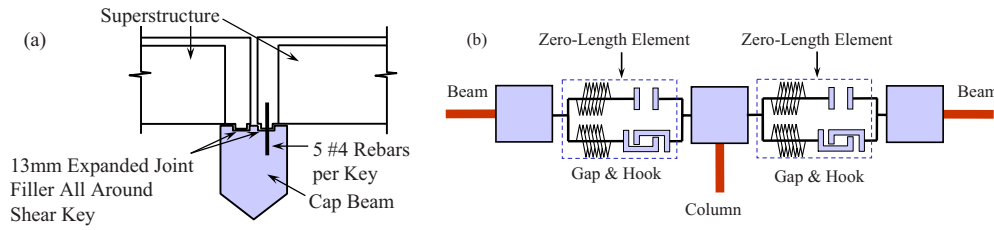**Figure 15.** Shear key at abutment joints: (a) as built, and (b) FE model.

Figure 16. Shear key at interior expansion joints: (a) as built, and (b) FE model.

models used to represent the shear keys were determined based on the construction drawings of the bridge and simplified design-type models of shear keys. These material parameters are reported in Table 5. Figure 18 shows a typical cyclic force-deformation response of a shear key.

BOUNDARY CONDITIONS OF COMPUTATIONAL SOIL DOMAIN AND DEFINITION OF SEISMIC INPUT

The major difficulty in directly including bounded soil layers into a FE model is that these bounded layers do not allow wave energy in the computational soil domain to propagate away. In reality, part of this energy propagates beyond the boundary of the computational domain, is dissipated by the soil medium outside this boundary and is never reflected back into the computational domain. Thus, soil modeling based on fixed (or spring supported) soil boundary conditions ignores radiation damping and introduces spurious wave reflections along boundaries of the computational soil domain. For numerical accuracy, the maximum dimension of any soil element must be limited to one-eighth through one-fifth of the shortest wavelength considered in the analysis. With this limitation, it is thus desirable, for computational efficiency, to decrease the overall size
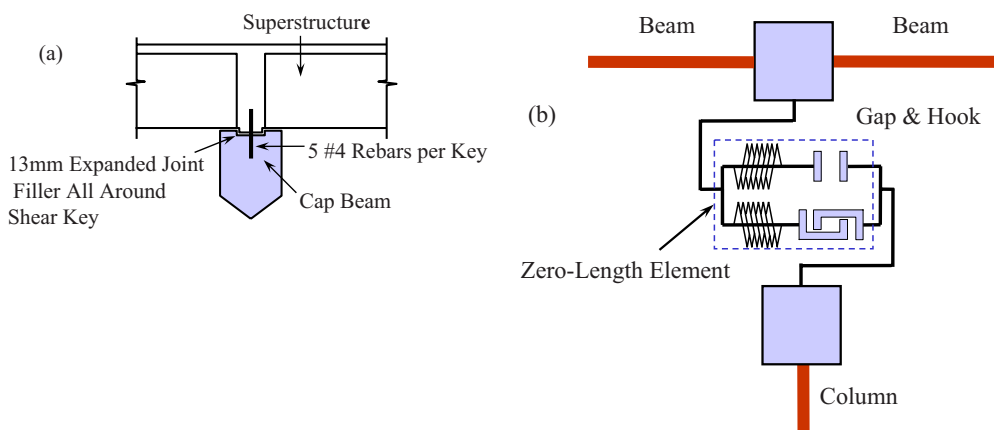

Figure 17. Shear key at continuous joints: (a) as built, and (b) FE model.

Table 5. Material parameters of shear keys

Shear key location	Type	Elastic stiffness (kN/m)	Yield strength (kN)	Width of gap or hook (mm)	Maximum deformation (mm)
Abutments	Gap	5.00×10^7	$-\text{Inf}$	-25.4	-102
	Hook	1.08×10^6	3700	12.7	102
Left shear key at interior expansion joints	Gap	8.50×10^5	-2200	-12.7	-102
	Hook	6.07×10^5	2100	12.7	102
Right shear key at interior expansion joints	Gap	1.72×10^6	-2100	0	-102
	Hook	1.82×10^6	2100	0	102
Continuous joints	Gap	1.62×10^5	-1350	0	-102
	Hook	1.62×10^5	1350	0	102

of the soil domain included in the FE model of the BFG system. As the overall size of the soil domain decreases, appropriate treatment of its boundary conditions becomes increasingly important. In the two-dimensional FE model presented here, it is assumed that the seismic response of the foundation soil is predominantly caused by vertically propagating plane shear waves. Bedrock below the computational soil domain is assumed to be a homogeneous, linear elastic, undamped semi-infinite half-space. The Lysmer-Kuhlemeyer (L-K) boundary (Lysmer and Kuhlemeyer 1969) is applied to eliminate spurious wave reflections at the soil mesh boundary (Zhang et al. 2003). Equivalent forces (Joyner 1975; Ayala and Aranda 1977) are used to represent the seismic input.

For one-dimensional vertical shear wave propagation through a homogeneous, linear elastic, undamped soil material, the wave equation is

$$\frac{\partial^2 u(x,t)}{\partial t^2} = v_s^2 \frac{\partial^2 u(x,t)}{\partial x^2} \tag{2}$$

where u denotes the soil particle displacement (perpendicular to the direction of wave propagation) and v_s denotes the shear wave velocity of the material given by

$$v_s = \sqrt{\frac{G}{\rho}} \tag{3}$$

in which G and ρ are the shear modulus and mass density of the material, respectively. The general solution of Equation 2 has the form

$$u(x,t) = u_r\left(t - \frac{x}{v_s}\right) + u_i\left(t + \frac{x}{v_s}\right) \tag{4}$$

where $u_r(\cdots)$ and $u_i(\cdots)$ can be any arbitrary functions of $(t-x/v_s)$ and $(t+x/v_s)$, respectively. The term $u_r(t-x/v_s)$ represents the wave traveling at velocity v_s in the positive x-direction (i.e., downwards), while $u_i(t+x/v_s)$ represents the wave traveling at the
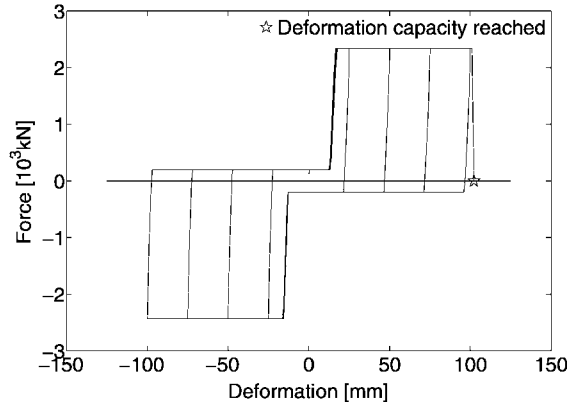
Figure 18. Typical cyclic force-deformation response of shear keys.

same speed in the negative x-direction (i.e., upwards or towards the ground surface). With x assumed positive downwards, u_i represents the incident wave traveling upwards into the computational soil domain, while u_r denotes the wave reflected downwards at the ground surface and transmitted through the base of the computational soil domain into the bedrock represented as a semi-infinite linear elastic half-space. Taking the partial derivative with respect to time of both sides of Equation 4 and multiplying by ρv_s yields

$$\rho v_s \frac{\partial u(x,t)}{\partial t} = \rho v_s u_r'\left(t - \frac{x}{v_s}\right) + \rho v_s u_i'\left(t + \frac{x}{v_s}\right) \tag{5}$$

where the prime superscript denotes the derivative of the associated function with respect to its argument. Assuming linear elastic material behavior, the shear stress $\tau(x,t)$ is given by

$$\tau(x,t) = G \frac{\partial u(x,t)}{\partial x} = -\frac{G}{v_s} u_r'\left(t - \frac{x}{v_s}\right) + \frac{G}{v_s} u_i'\left(t + \frac{x}{v_s}\right) \tag{6}$$

By substituting $G = \rho \cdot v_s^2$ into Equation 6, the latter can be rewritten as

$$\tau(x,t) = -\rho v_s u_r'\left(t - \frac{x}{v_s}\right) + \rho v_s u_i'\left(t + \frac{x}{v_s}\right) \tag{7}$$

Finally, combining Equations 5 and 7 yields

$$\tau(x,t) = -\rho v_s \frac{\partial u(x,t)}{\partial t} + 2\rho v_s u_i'\left(t + \frac{x}{v_s}\right) \tag{8}$$

This is the same expression reported by Ayala and Aranda (1977). Note that $\partial u(x,t)/\partial t$ represents the velocity of the total soil particle motion, while $u_i'(t+x/v_s)=\partial u_i(t+x/v_s)/\partial t$ is the velocity of the incident soil particle motion. Therefore, according to Equation 8, the shear stress at any point of a linear elastic soil column can be expressed as the summation of two terms. The first term is equivalent to a force (per unit area) generated by a viscous damper with a constant damping coefficient ρv_s (per unit area), while the second term is given by a force (per unit area) proportional to the velocity of the incident soil particle motion. As a result, the soil (assumed homogeneous, linear elastic, undamped) below that point (considered at the boundary between the computational soil domain and the bedrock) can be replaced with a dashpot and an equivalent force, which defines the seismic input at the base of the computational soil domain. This treatment of the boundary conditions allows transmission, without reflection, of the vertically incident seismic waves and descending waves (after reflection at the ground surface) through the base boundary of the computational soil domain, thus accounting for radiation damping. This modeling approach assumes that the bedrock underlying the bridge site is made of homogeneous, linear elastic, undamped material. There is no spatial variability of the incident wave motion at bedrock level based on the assumption of vertically propagating plane shear waves. At each node along the base and lateral boundaries of the soil domain, a horizontal dashpot is set to transmit the shear waves (at the base) and compressive waves (at the lateral boundaries), respectively. The coefficient of the dashpots at the base is $\rho v_s A$, while that of the dashpots on the lateral boundaries is $\rho v_p A$, where ρ, v_s and v_p denote the mass density, shear wave velocity, and compressive wave velocity, respectively, of the soil material outside the boundary (i.e., bedrock), and A is the tributary surface area of the corresponding node. The earthquake excitation is applied as equivalent horizontal forces at the nodes along the base of the computational soil domain. Seismic inputs, however, are usually expressed in terms of accelerograms recorded at the free-field ground surface. Consequently, the free-field motion considered needs to be deconvolved in order to obtain the corresponding incident wave motion at the base of the computational soil domain.

Deconvolution of the free-field ground motion records downwards to the bedrock level consists of computing the incident vertical shear wave motion at bedrock level that causes the specified free-field motion after propagation through the deformable soil layers between bedrock and ground surface. A one-dimensional soil column with five horizontal layers, matching the soil profile at the center of the river channel, was used to deconvolve the free-field surface motions using SHAKE91 (Idriss and Sun 1993). This program computes the response of a system defined by homogeneous, visco-elastic layers of infinite horizontal extent subjected to vertically traveling shear waves. It is based on the continuous solution to the wave equation adapted for use with transient motions through the Fast Fourier Transform algorithm. The nonlinearity of the soil behavior, manifested by a shear modulus and damping ratio that depend on the magnitude of the effective shear strain at a given point in the soil, is accounted for by the use of equivalent linear soil properties through an iterative procedure to obtain values for shear modulus and damping ratio that are compatible with the effective shear strain in each layer. The shear modulus reduction and damping curves of sand (Figure 19) as well as the deconvolution procedure recommended by Silva (2003) were used in this study.
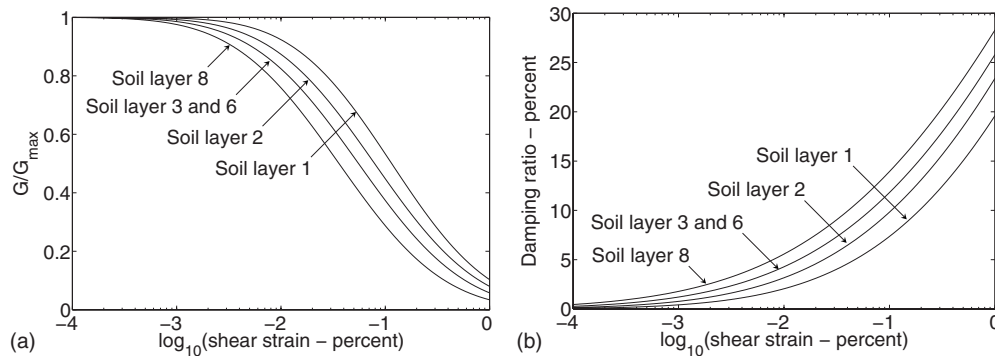
Figure 19. Shear modulus reduction and damping curves used in deconvolution (Silva 2003).

INERTIA AND DAMPING PROPERTIES

The mass of the structure is calculated based on the density and volume of structural components and is lumped at the nodes of the structural model. Rotatory inertia effects are neglected. The total translational mass at any node corresponds to the sum of the nodal contributions from all elements attached to that node. A concrete mass density of 2400 kg/m^3 is assumed. In this study, the bridge is assumed in its bare condition (without any traffic load), and therefore no traffic related inertia effects are considered. For the various soil layers, the buoyant soil density is used to compute gravity loads, while the saturated soil density (i.e., including both soil and water) is used to calculate the inertia forces induced by earthquake excitation. The saturated unit weights of the various soil layers are given in Table 1.

The various sources of damping (or energy losses) in structures are mainly due to: (1) internal hysteresis in materials arising from nonlinear stress-strain behavior, intergranular friction and thermoelasticity; (2) friction in sliding of joints, supports, cladding or various other parts of the structure during relative motion; and (3) radiation damping at the supports of the structure (i.e., the vibration of the structure strains the foundation soil near the supports and causes stress waves to radiate into the infinite foundation soil). Generally, modal damping or Rayleigh damping (both linear viscous damping) is used in order to approximate unknown nonlinear energy dissipation when simulating the dynamic response of a structure (Clough and Penzien 2003). However, in the model of the BFG system presented here, nonlinear constitutive models are adopted for the various materials or components, such as concrete, reinforcing steel, soil, and shear keys; the friction between the superstructure and the bridge piers/abutments is represented as described in the section on Shear Keys at Expansion and Continuous Joints, and the radiation damping is incorporated by direct inclusion of the foundation soil layers and application of the L-K boundary in the FE model. Thus, most of the sources of damping in the BFG system have been explicitly accounted for in the present model. Furthermore, bridge structures (without foundation and soil substructures) are well known for their absence of damping capacity. Damping values of bridge structures can be as low as the

inherent material damping in some cases, although generally there are quite wide variations, chiefly due to relative motions at the supports (Eyre and Tilly 1977). Therefore, based on the above considerations, no additional modal/Rayleigh damping was incorporated in the FE model so as to avoid artificial excessive energy dissipation in the model of the BFG system, especially in light of the fact that, as already mentioned, a 2-D representation of the soil foundation over-estimates the radiation damping associated with low frequency modes.

STAGED ANALYSIS PROCEDURE

Since pressure dependent elastoplastic material constitutive models are used to simulate the behavior of some soil layers, lateral confinement is needed for these soil layers to develop some initial strength. However, the dashpots along the L-K boundaries of the computational soil domain cannot provide any lateral static constraint. Therefore, in order to conduct a seismic response analysis of the nonlinear BFG system, the following staged analysis procedure is followed. (1) The FE mesh of the soil domain only, including the abutments, is created with its base fixed in both the horizontal and vertical directions and lateral boundaries fixed in the horizontal direction only. The various soil constitutive models are set as linear elastic, and soil gravity is applied statically in a single linear elastic analysis step. (2) The soil constitutive models are switched from linear elastic to elastoplastic (with liquefaction effects incorporated) using the *updateMaterialStage* command in OpenSees, which is unique to the soil models used herein. Then, the new static equilibrium state under soil gravity is obtained iteratively. (3) The nonlinear model of the bridge superstructure, piers and pile group foundations is added to the soil mesh and bridge gravity is applied statically to the nonlinear model of the BFG system. (4) All horizontal displacement constraints along the base and lateral boundaries of the soil domain are removed and replaced with the corresponding support reactions recorded at the end of the previous stage of analysis. After confirming that static equilibrium under gravity load is still satisfied, a horizontal dashpot is added to each node along the boundaries of the computational soil domain to implement the L-K boundary conditions. (5) Finally, from the static equilibrium configuration under gravity loads, the seismic excitation is applied in the form of equivalent horizontal nodal forces applied along the base of the computational soil domain as defined earlier.

SMALL AMPLITUDE VIBRATION ANALYSIS

Since the BFG model has no horizontal displacement restraints after the L-K boundary conditions are implemented, its global static stiffness matrix is singular. Thus, conventional eigensolvers can not be applied to the model to determine its eigenvalues and eigenvectors. In order to study the natural vibration characteristics of the nonlinear system corresponding to its initial stiffness properties (after application of gravity loads), it is necessary to linearize the material properties of the BFG model. In this study, linearization of the system after application of the gravity load was achieved by applying small amplitude dynamic excitations to the BFG model. The amplitude of these excitations was made sufficiently small (peak ground acceleration of the order of 1 mm/sec2) such that the system response remains quasi-linear. A check of quasi-linearity was per-
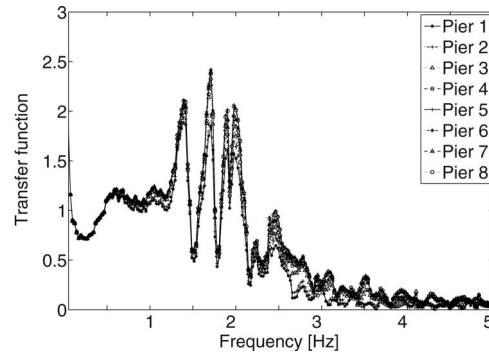
Figure 20. Transfer functions of BFG system between incident seismic wave particle velocity (input) and total horizontal displacement at pier tops (outputs).

formed for global response quantities (e.g., pier lateral drifts) by verifying that these response quantities are exactly doubled for double amplitude excitations. The natural frequencies of the system were then obtained from transfer functions between inputs and outputs. Comparison of the transfer functions obtained for different excitations indicates that they are in good agreement. Figure 20 shows the transfer functions between the incident seismic wave particle velocity (to which the equivalent seismic forces applied at the base of the computational soil domain are proportional) and the total horizontal displacement of the top of all piers. The transfer functions are characterized by two low and broad spectral peaks at 0.60 Hz and 1.05 Hz, respectively, four high and narrow spectral peaks at 1.40 Hz, 1.70 Hz, 1.90 Hz and 1.98 Hz, respectively, and other smaller spectral peaks above 2.0 Hz; and they become negligibly small beyond 5.0 Hz. Figure 21
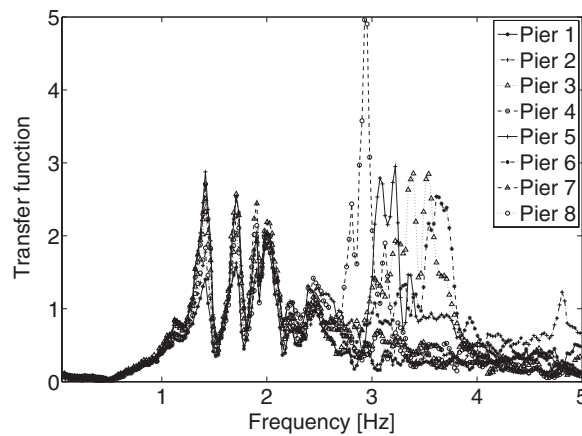
Figure 21. Transfer functions of BFG system between incident seismic wave particle velocity (input) and pier lateral drifts (outputs).
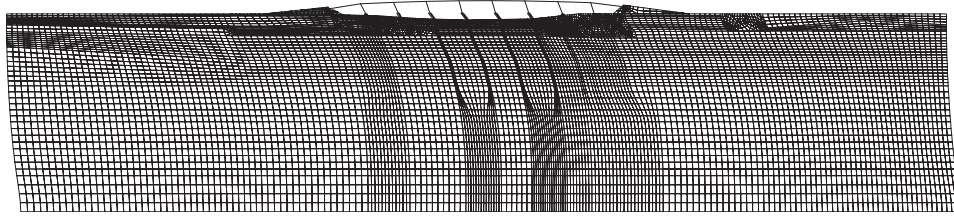
Figure 22. Mode I of the BFG system ($f_I = 1.40$ Hz).

shows the transfer functions between the incident seismic wave particle velocity and the lateral drift of all piers. It is noteworthy that these transfer functions are almost zero below 0.5 Hz and have four high and narrow spectral peaks at the same frequencies (1.40 Hz, 1.70 Hz, 1.90 Hz, and 1.98 Hz) as the previous transfer functions. This indicates that the previous transfer functions below 1 Hz, including the two spectral peaks at 0.60 Hz and 1.05 Hz, are primarily contributed by motion of the foundation soil (with very small contribution from the bridge deformation). Single harmonic excitations of frequencies 0.60 Hz, 1.05 Hz, 1.40 Hz and 1.70 Hz, respectively, were applied to the BFG model, in order to examine the system mode shapes corresponding to these frequencies. The model displacement responses to these harmonic excitations were animated using GID. It was observed that the bridge moves rigidly with the foundation soil for the harmonic excitation at 0.60 Hz, and moves very slightly relative to the foundation soil for the harmonic excitation at 1.05 Hz. In the case of the harmonic excitation at 1.40 Hz, the bridge superstructure vibrates with large motion relative to and in phase with the foundation soil (Figure 22), while it vibrates with large motion out of phase with the foundation soil for the excitation at 1.70 Hz (Figure 23). Thus, these last two modes ($T_I = 0.71$ sec and $T_{II} = 0.59$ sec) represent the lowest two system vibration modes with significant participation from both the foundation soil and the bridge structure.

In order to study the effects of SSI on the natural frequencies of the bridge, a FE model of the bridge structure only down to the pile caps was developed and its transfer functions were also determined. This model is identical to its counterpart in the BFG model, except that it is fixed (i.e., zero translations and zero rotation) at the base of each
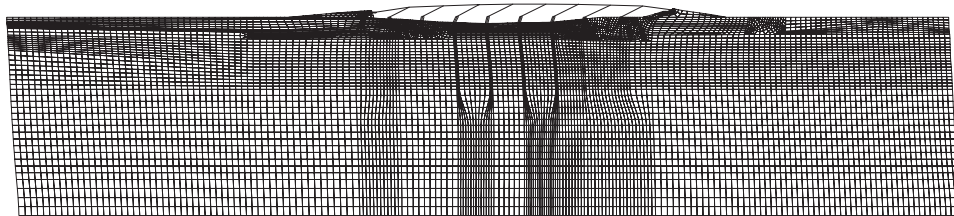

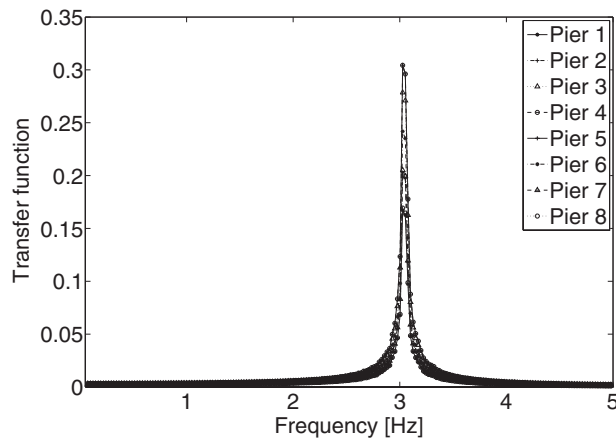**Figure 23.** Mode II of the BFG system ($f_{II} = 1.70$ Hz).

Figure 24. Transfer functions of bridge structure only between rigid soil acceleration (input) and pier lateral drifts (outputs).

pier and at the abutment end of the shear keys at both abutments (see Figure 15). Horizontal rigid soil excitations were applied to the bridge model. Again the amplitude of these excitations was made sufficiently small to ensure quasi-linearity of the bridge response. Figure 24 shows the transfer function between the rigid soil acceleration (input) and the pier lateral drift response (output) for each pier. As can be seen, the transfer functions of all piers have one peak at the same frequency 3.03 Hz, which matches the fundamental frequency of the bridge model, 3.05 Hz, obtained through eigen-analysis. Thus, the fundamental frequency of the bridge decreases from 3.03 Hz to 1.40 Hz for the combined BFG system reflecting SSI effects. It is also noteworthy that the transfer functions of all piers in the model of the bridge on rigid soil have the same shape (see Figure 24), while those of the piers in the model of the BFG system have the same shape below 2.5 Hz but differ significantly above 2.5 Hz (see Figure 21). This is due to wave propagation effects in the computational soil domain, causing different ground surface motions at the base of the piers.

EARTHQUAKE RESPONSE ANALYSIS

In the earthquake response analysis presented below, only gravity loads and seismic excitation are considered; live traffic loads are ignored. Two recorded free-field earthquake ground motions are used to derive the seismic input to the BFG model for studying its behavior during earthquakes of different intensities. The first earthquake (Earthquake #1) corresponds to the fault-parallel component (215° E of N) of 26 April 1992 Cape Mendocino aftershock ($M_w=6.6$) recorded at Bunker Hill station, while the second earthquake (Earthquake #2) is given by the fault-parallel component (10°E of N) of 3 May 1985 Valparaiso, Chile earthquake ($M_w=8.0$) recorded at Pichilemu station (Somerville and Collins 2002). These two earthquake records are scaled to match the 5% damped elastic spectral acceleration at the fundamental period of the BFG system
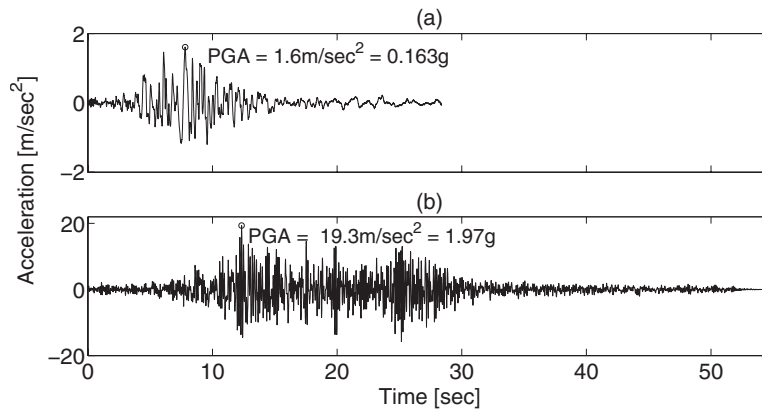
Figure 25. Scaled free-field earthquake records used in this study: (a) fault-parallel component (215°E of N) of the 26 April 1992 Cape Mendocino aftershock (Mw=6.6) recorded at the Bunker Hill station; (b) fault-parallel component (10°E of N) of the 3 May 1985 Valparaiso, Chile earthquake (Mw=8.0) recorded at the Pichilemu station.

(T_I=0.71 sec) corresponding to a probability of exceedance (PE) of 50% in 50 years (annual PE of 1.4%, return period=72.5 years) for Earthquake #1 and 2% in 50 years (annual PE of 0.040%, return period=2,475 years) for Earthquake #2. The scaling factors applied are 1.8 and 7.1 for Earthquakes #1 and 2, respectively. Figure 25 shows the scaled version of these two free-field historical earthquake records used in this study. Their peak ground accelerations (PGA) are 1.6 m/sec^2 (0.163 g) and 19.3 m/sec^2 (1.97 g), respectively, while their 5% damped elastic spectral accelerations at T_I=0.71 sec are 0.46 g and 1.75 g, respectively. These two ground motions are both recorded on rock site as rock outcrop motions. Therefore, the deconvolution can be simplified by the fact that in the case of vertically propagating shear waves in a homogeneous undamped linear elastic half-space, the amplitude of the total free surface motion is twice the amplitude of the incident motion at any point in the half-space (Kramer 1996). As a result, for each earthquake, the incident seismic wave motion is taken as half the scaled free-field ground motion and is then applied to the BFG model following the staged analysis procedure described above.

Soil Response: Figure 26 shows the locations of two control soil columns, eight soil nodes on the ground surface and three soil elements (at locations A, B, and C), at which the soil response is examined. Figures 27 and 28 show the shear stress vs. shear strain hysteretic response and excess pore pressure ratio response histories at locations A, B and C in the foundation soil during Earthquakes #1 and #2, respectively. The excess pore pressure ratio is defined here as the excess pore pressure (above the hydrostatic pore pressure) over the mean effective soil pressure under gravity alone. The soil materials at locations A and B are modeled with pressure dependent and pressure independent constitutive models, respectively; while at location C, the soil is modeled as a pressure dependent material and is located in soil layer 5, which is susceptible to liquefaction under
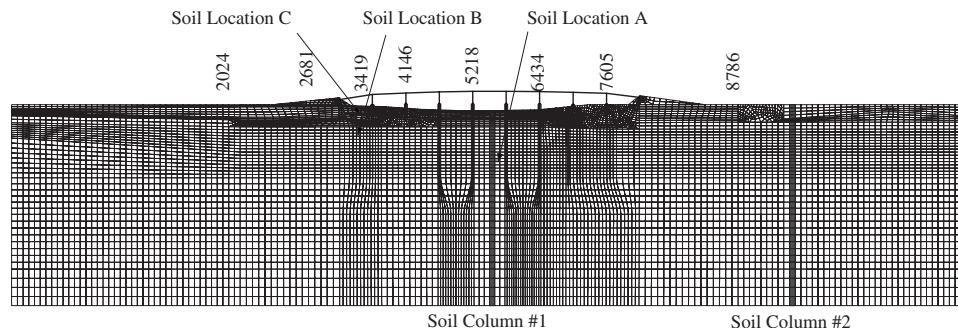
Figure 26. Control soil columns, soil locations, and soil nodes along the ground surface.

strong ground shaking. As shown in Figure 27, the hysteresis loops at the three soil locations A, B, and C are very narrow for Earthquake #1 indicating low level of inelasticity; while during Earthquake #2 the soil response is highly nonlinear. It can be seen from Figure 28 that the excess pore pressure gradually builds up until the end of the strong motion phase of the seismic input at all three locations during both earthquakes and that the soil at location C reaches liquefaction during Earthquake #2. Consequently, the soil at location C undergoes dramatic strength deterioration and stiffness degradation when approaching and after reaching liquefaction during Earthquake #2. In comparison, the soil materials at locations A and B do not exhibit significant losses of strength and stiffness.

Figures 29–32 show the total horizontal and vertical acceleration response histories as well as the profiles of the peak and root-mean-square (RMS) of the total horizontal acceleration (THA) along the height of the two control soil columns (see Figure 26) during Earthquakes #1 and #2, respectively. The peak and RMS total horizontal acceleration follow the same trend along soil column height. It is observed that the vertical acceleration is consistently very small compared to the horizontal acceleration. Thus, irregular soil stratification and surface topography do not result in any appreciable vertical soil response in the present case. During Earthquake #1, it is observed that the THA amplifies as the seismic waves travel upwards. The peak THA is in the range $0.9-1.0$ m/sec^2 at the base of the soil domain and $2.5-2.6$ m/sec^2 at the ground surface (see Figures 29a and 30a). The profile of the peak THA along column height is similar for both soil columns (see Figures 29b and 30b). It is also found that the shear stress versus shear strain hysteresis loops along the height of both soil columns remain narrow (with narrowness increasing with depth), except near the ground surface (top 2 m of soil), indicating that the various soil layers below the surficial soil layer (layer 8 in Figure 3) respond quasi-linearly. As expected from one-dimensional elastic wave propagation, significant amplification is observed as the waves approach the ground surface due to constructive interference of the upwards- and downwards-propagating (incident and reflected) wave components. During Earthquake #2, the peak THA along the height of soil column #1 decreases from 11.0 m/sec^2 at the base of soil layer 1 to a minimum of 6.0 m/sec^2 150 m above (still in soil layer 1), increases to 8.0 m/sec^2 in soil layer 2,
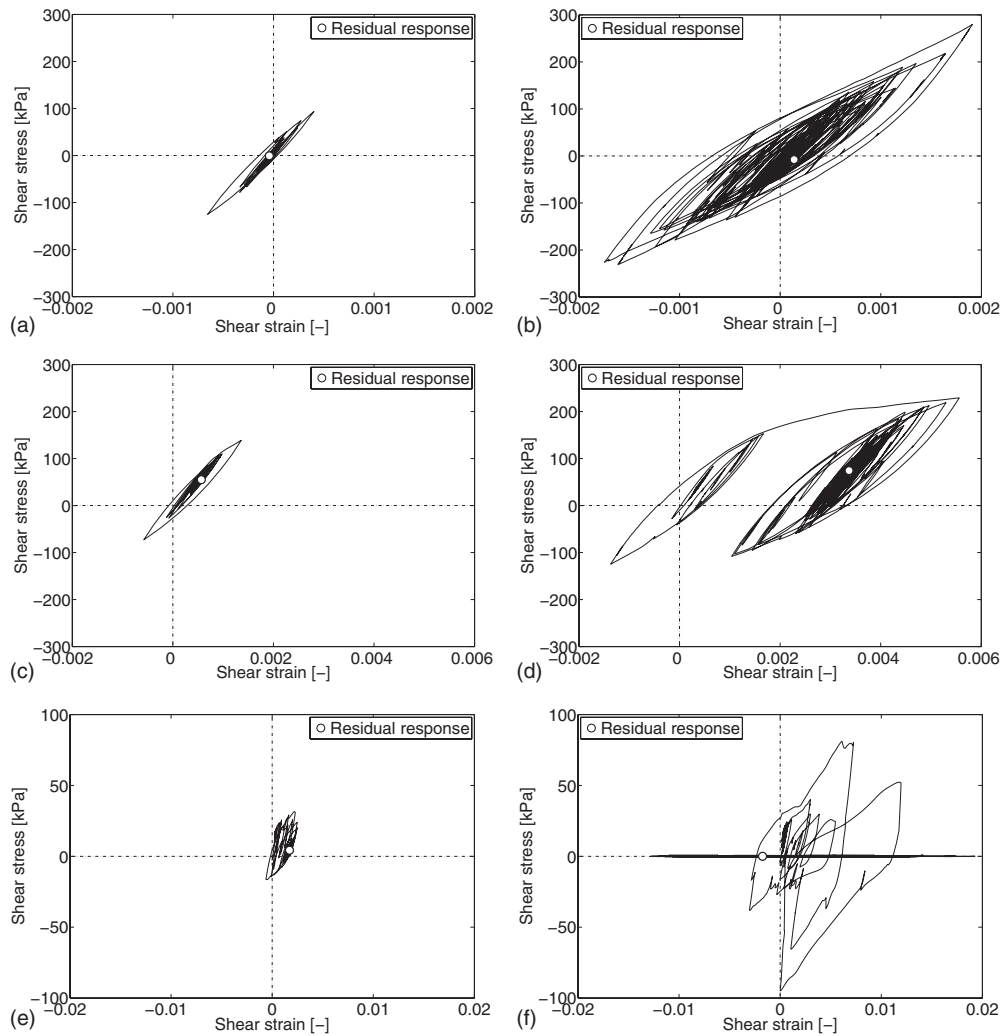
Figure 27. Shear stress vs. shear strain hysteretic response at soil locations A, B, and C: (a) soil location A, Earthquake #1, (b) soil location A, Earthquake #2, (c) soil location B, Earthquake #1, (d) soil location B, Earthquake #2, (e) soil location C, Earthquake #1, and (f) soil location C, Earthquake #2.

and increases dramatically across soil layers 3, 4, 6 and 8 (see Figure 3), to reach 21.8 m/sec^2 on the ground surface (Figure 31). It is observed that the frequency bandwidth of the THA is significantly higher in the top soil layers (layers 2, 3, 4, 6 and 8) than in the bottom soil layer (soil layer 1) due to an increase in soil response nonlinearity in these layers (strain softening and subsequent hardening due to dilation at large shear strain near the ground surface where soil shear stiffness and strength are relatively small). The peak THA along the height of soil column #2 undergoes the same trend
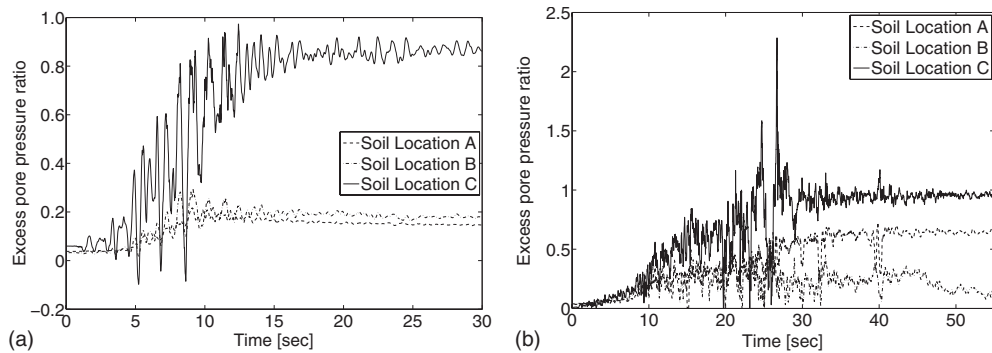
Figure 28. Time histories of excess pore pressure ratio at soil locations A, B and C: (a) Earthquake #1, and (b) Earthquake #2.

across soil layers 1, 2, and 3 as in soil column #1. However, in contrast with soil column #1, the THA is not amplified, but reduced across the top soil layers 5, 7, and 8 (see Figure 3) to reach a peak THA of only 6.6 m/sec^2 on the ground surface (Figure 32). Plots of shear stress versus shear strain hysteresis loops and excess pore pressure time histories (not shown here due to space limitation) indicate that liquefaction occurs in soil layer 5 (similar to soil location C in Figures 27 and 28) resulting in drastic reduction in shear strength and stiffness. This shear strength degradation acts as an isolation mechanism (base-isolator effect) for the soil layers (7 and 8) above the liquefied layer. More specifically, the reduced strength of the liquefied layer limits the force/acceleration that can be transmitted to the overlaying soil layers and its reduced stiffness filters out the high frequency components as clearly shown in Figure 32a (nodes 11 and 12).

Figures 33 and 34 show the recorded free-field ground acceleration used to derive
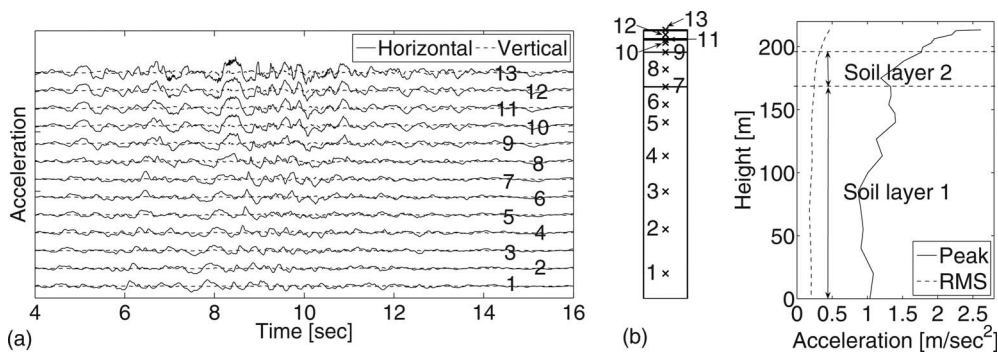
Figure 29. (a) Soil total horizontal and vertical acceleration response to Earthquake #1 along the height of soil column #1, and (b) profiles of peak and root-mean-square total horizontal acceleration along the height of soil column #1.
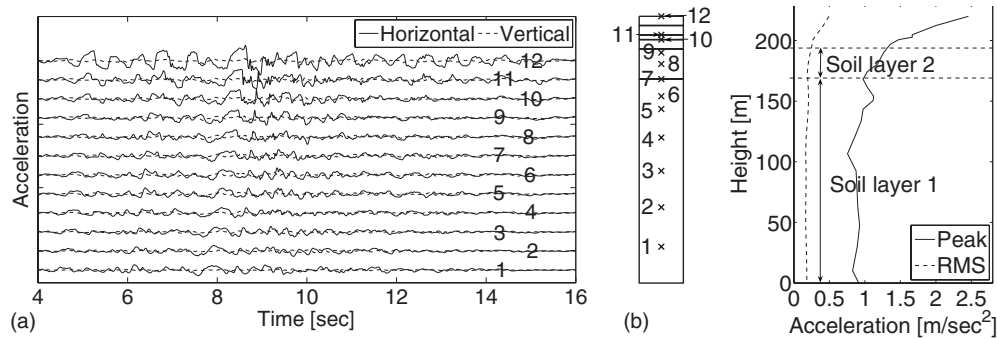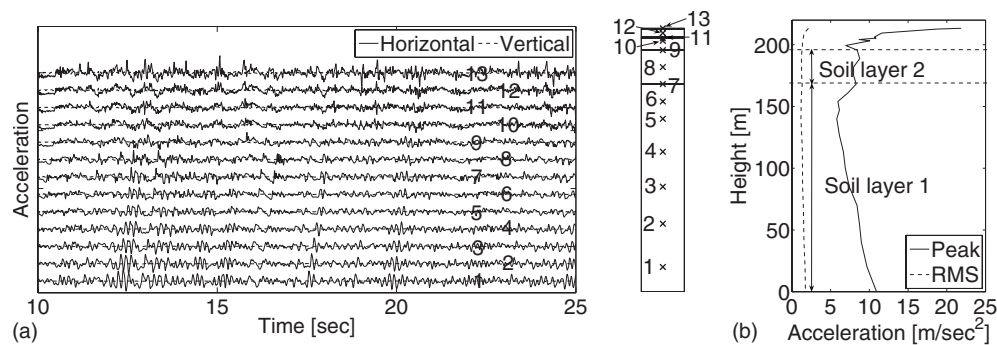
Figure 30. (a) Soil total horizontal and vertical acceleration response to Earthquake #1 along the height of soil column #2, and (b) profiles of peak and root-mean-square total horizontal acceleration along the height of soil column #2.

the seismic input (parent free-field surface motion) and the simulated THA response at eight control points on the ground surface (shown in Figure 26) during Earthquake #1 and #2, respectively. Figure 35 displays the 5 percent damped linear elastic pseudo-acceleration response spectra corresponding to the parent free-field record and the simulated surface ground acceleration at several control points. From Figures 33–35, it is observed that the amplitude and frequency content of the surface ground acceleration can vary significantly from location to location during the same earthquake, especially when the soil undergoes significant nonlinear response (as in Earthquake #2). This illustrates the importance of local site condition and surface topography. It is also seen that for Earthquake #1, the overall amplitude of the simulated horizontal ground surface acceleration is larger than that of the parent recorded free-field motion, whereas this relation is inverted for Earthquake #2. This is consistent with the distinct trends in amplification

Figure 31. (a) Soil total horizontal and vertical acceleration response to Earthquake #2 along the height of soil column #1, and (b) profiles of peak and root-mean-square total horizontal acceleration along the height of soil column #1.
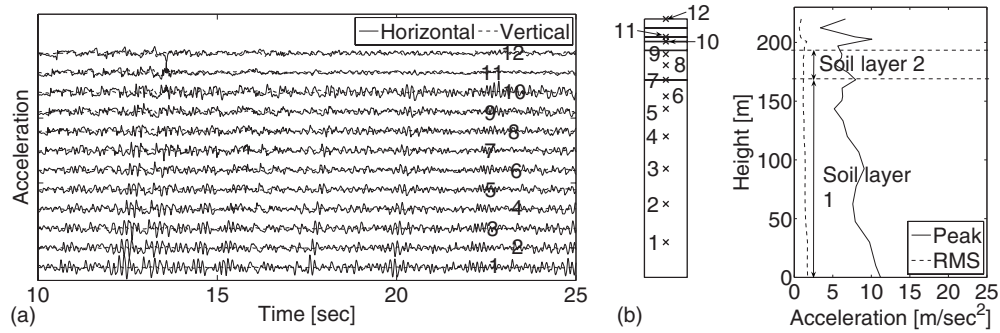
Figure 32. (a) Soil total horizontal and vertical acceleration response to Earthquake #2 along the height of soil column #2, and (b) profiles of peak and root-mean-square total horizontal acceleration along the height of soil column #2.

behavior of soil sites observed by other researchers (Seed et al. 1976; Idriss 1990). They found that at low to moderate acceleration levels (less than about 0.4 g), peak accelerations at soft sites are likely to be greater than those on rock sites. At higher acceleration levels, however, the low stiffness and nonlinearity of soft soils often prevent them from developing peak ground accelerations as large as those measured on rock.

Figure 36a shows a color map of the soil shear stress ratio of the BFG system at $t = 10.22$ sec into Earthquake #2. Here, the shear stress ratio is defined as the octahedral shear stress demand over the shear strength under the current confinement pressure (i.e., mean normal effective stress). Soil elements that have reached their shear strength are denoted in dark red. Clearly, at this instant, a large portion of the foundation soil is un-
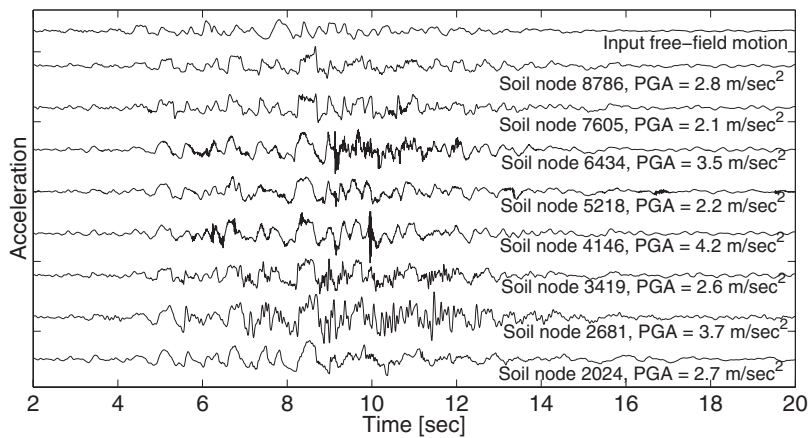

Figure 33. Total horizontal acceleration response histories along the ground surface for Earthquake #1.
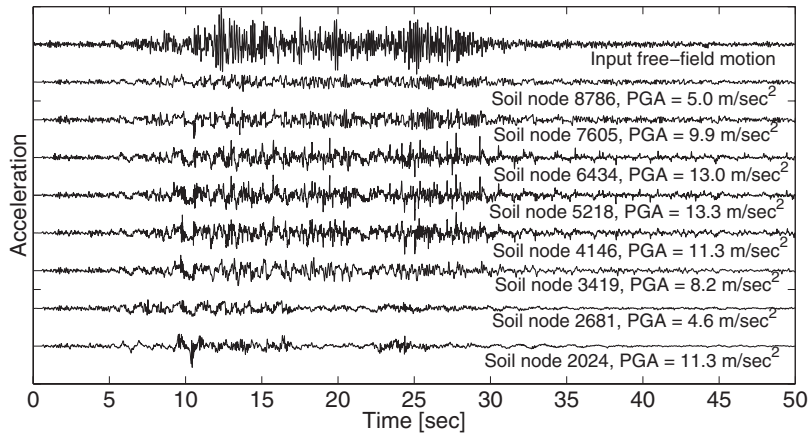
Figure 34. Total horizontal acceleration response histories along the ground surface for Earthquake #2.

dergoing intense shearing, and the shear stress ratio decreases overall with depth. The shear stress demand under the abutments and near the pile foundations is near the shear strength. The shear stress in soil layer 5 (see Figure 3) on both sides of the bridge also nears the shear strength due to large build up of the pore water pressure. The response of the soil only (without the presence of the bridge) to Earthquake #2 was also computed. Figure 36b shows the same color map, but of the soil-only system (even though the bridge is still shown to facilitate the comparison) at the same instant $t = 10.22$ sec. As can be seen, the spatial distributions of the shear stress ratio in the soil domain with and without the presence of the bridge are very similar, with some differences only near the abutments and pile foundations. This close similarity was observed at all times during the earthquake. The soil total horizontal displacement response histories at the locations
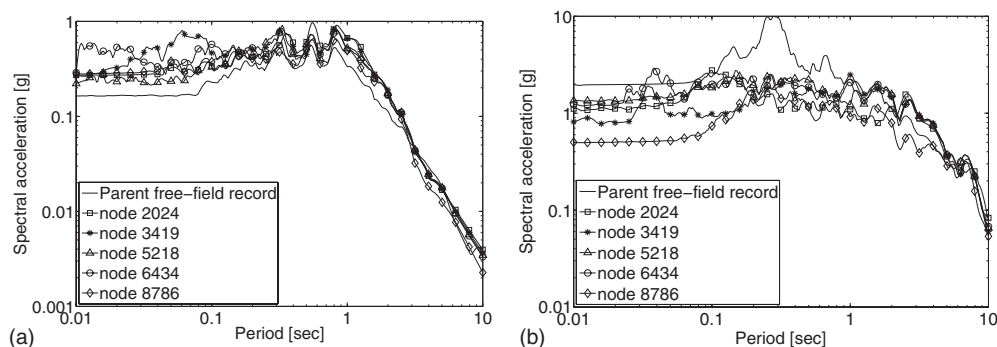

Figure 35. Spectral acceleration (5 percent damped) of parent free-field record and simulated surface ground acceleration at various control points: (a) Earthquake #1 and (b) Earthquake #2.
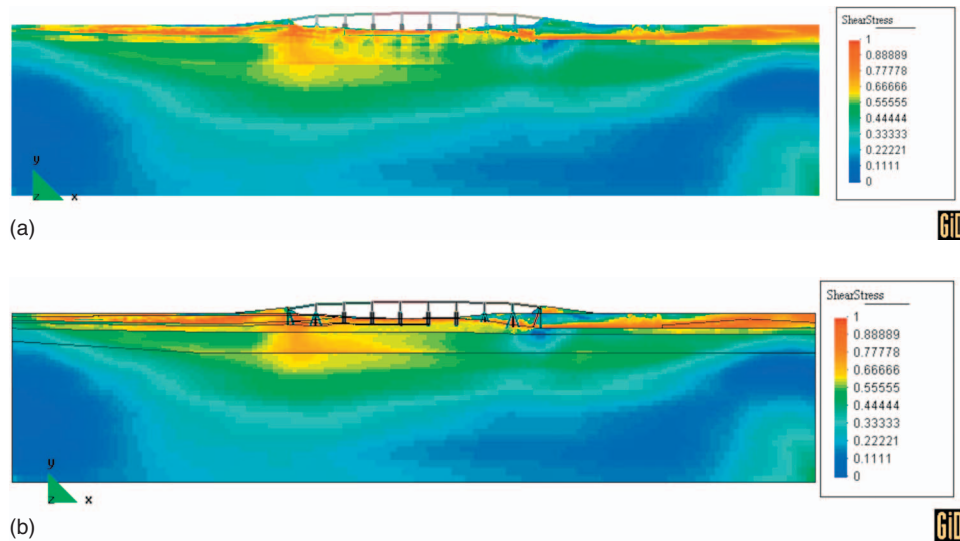
Figure 36. Shear stress ratio at t=10.22 sec into Earthquake #2: (a) BFG system and (b) soil-only system.

corresponding to the base of bridge piers #1 and 4 in the BFG system and in the soil-only system are shown and compared in Figure 37 for both Earthquakes #1 and #2. At each of the other pier base locations, the soil horizontal responses in the BFG system and soil-only system were also found quite similar, especially in the middle of the river channel and with the largest discrepancy near the abutments (i.e., Piers #1 and 8). On the other hand, as shown in Figure 38, the rotation of the soil on the ground surface near the pier bases is significantly affected by the presence of the bridge. Specifically, Figure 38 shows for Piers #1 and 5 the rotation response history of the pier base (base node of the pier) and of a horizontal soil line near the pier base in the BFG system and soil-only system, respectively. The rotation of each of the soil lines is obtained by taking the difference between the vertical displacements at the end nodes of the soil line and dividing it by the length of the soil line. Thus, the modification in the ground motion due to the presence of the bridge structure and its foundations with respect to the free field ground motion (soil-only system) is a manifestation of the soil-structure-interaction (SSI) that occurs in the system during the earthquake response. This interaction occurs primarily in the rocking at the base of the piers. It was found that the difference in the ground surface rotation near the pier bases between the BFG system and the soil-only system produces a noticeable difference in the bridge response. However, the extent of the effects of SSI appears to lessen significantly between the linear behavior of the BFG system under small earthquake excitation (decrease of fundamental bridge frequency from 3.03 Hz to 1.40 Hz) and its highly nonlinear behavior under very strong earthquake excitation. Possible decrease of SSI effects with increasing system nonlinearity was also previously reported by Bielak (1978).
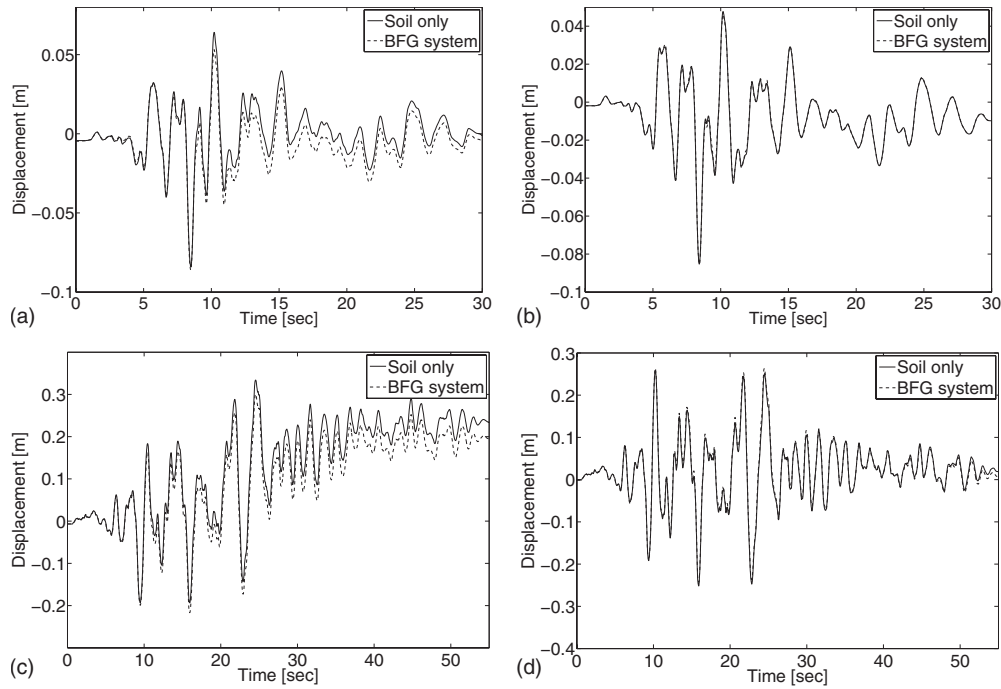
Figure 37. Comparison of soil total horizontal displacement response histories at locations corresponding to the base of the bridge piers (a) Pier #1, Earthquake #1, (b) Pier #4, Earthquake #1, (c) Pier #1, Earthquake #2, and (d) Pier #4, Earthquake #2.
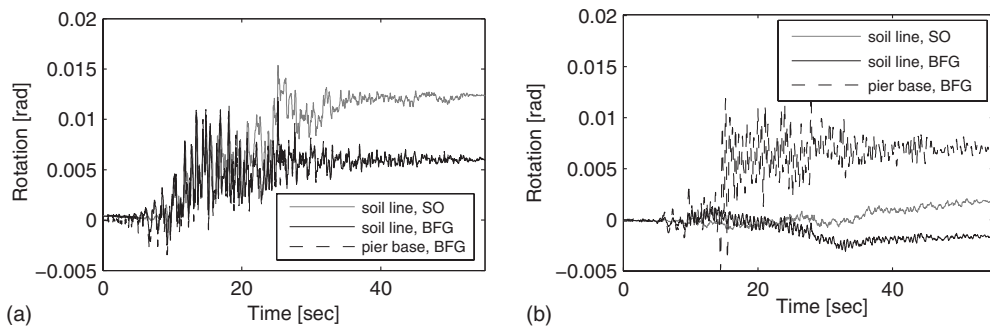

Figure 38. Comparison of rotation response histories of soil line in BFG system and soil only (SO) system and pier base in BFG system: (a) Pier #1 and (b) Pier #5.
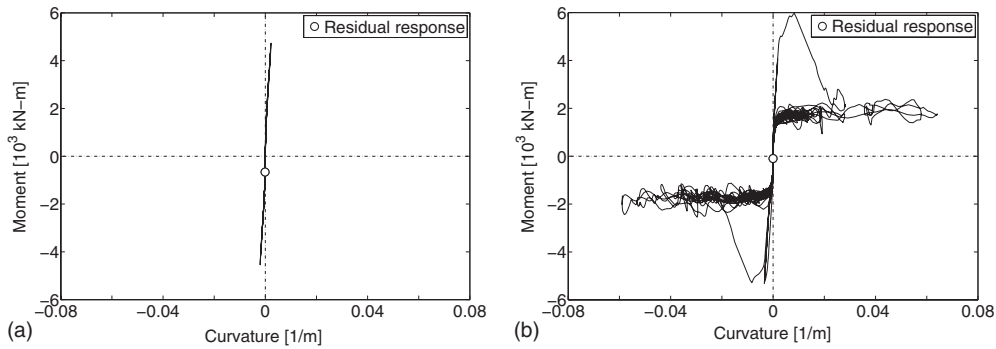
Figure 39. Moment-curvature response at base cross section of Pier #3 for (a) Earthquake #1 and (b) Earthquake #2.

Bridge Response: Figure 39 shows the moment-curvature response at the base cross section (spliced) of Pier #3 to Earthquake #1 and #2, respectively. As can be seen, the response to Earthquake #1 is quasi-linear, while the lap-spliced failure mechanism is fully developed during Earthquake #2 (i.e., flexural capacity has been reached with pier rocking on pile cap). Examination of the simulation results for the response of the piles shows that the piles remain quasi-linear during both earthquakes, although they are close to yielding in Earthquake #2.

Figure 40 shows the total horizontal displacement response histories of all pier tops during Earthquake #1 and #2, respectively. It is observed that these response histories for all 8 piers fall into three groups during both earthquakes. This is due to the fact that the bridge structure consists of three frames interconnected through shear keys with gaps at the two interior expansion joints as already explained earlier. Pier-tops in the same frame have almost identical total horizontal displacements due to the high axial stiffness of the
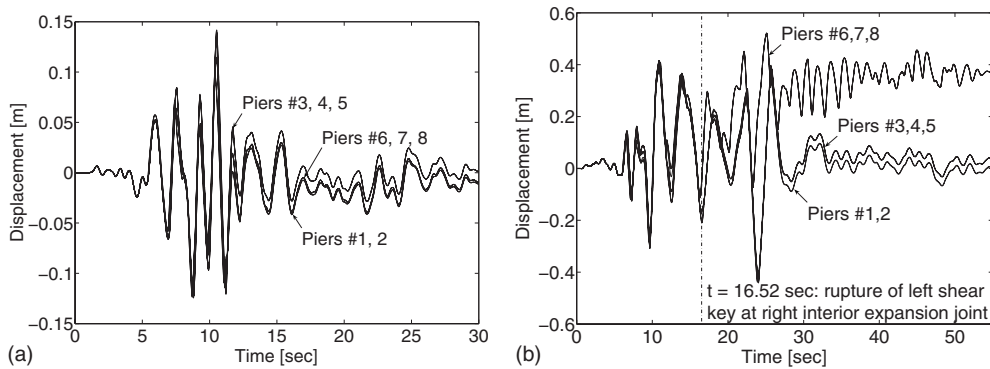

Figure 40. Total horizontal displacement response histories of all pier tops: (a) Earthquake #1 and (b) Earthquake #2.
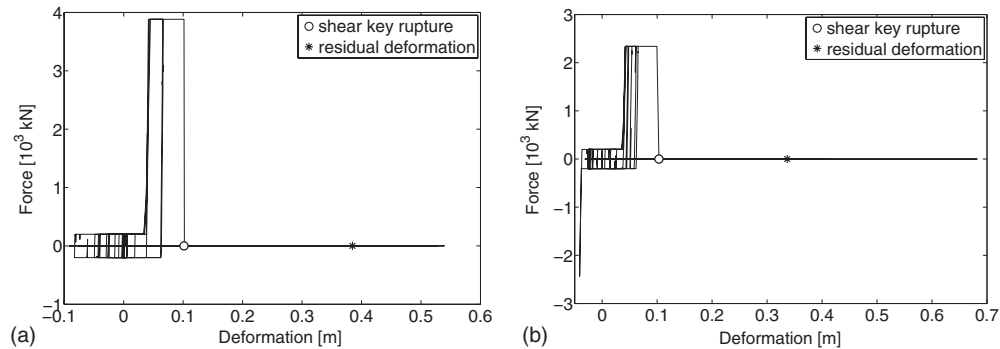
Figure 41. Force-deformation response of shear keys at (a) left abutment, and (b) right interior expansion joint (left shear key), during Earthquake #2.

bridge superstructure (girders and slab). In Earthquake #1, no shear key fails. Therefore, the difference in total horizontal displacement among the three response groups remains small (see Figure 40a). However, during Earthquake #2, the shear key at the left abutment and the left shear key at the right interior expansion joint (above Pier #6) rupture at $t=10.50$ sec and $t=16.52$ sec, respectively, as shown in Figure 41. After the shear key failure at the interior expansion joint, the right frame undergoes significant horizontal displacement relative to the other two frames (see Figure 40b). Unseating may occur at those joints where shear keys fail (i.e., reach their ultimate deformation capacities). The time history of the relative horizontal displacement between superstructure (girders) and abutment or pier top at the left abutment and right interior expansion joint are plotted in Figure 42 for Earthquake #2. The unseating limit, taken as the full width of the abutment seat or half the width of the pier, is also represented in Figure 42. It is observed that the peak (positive) relative horizontal displacement between the superstructure and left abut-
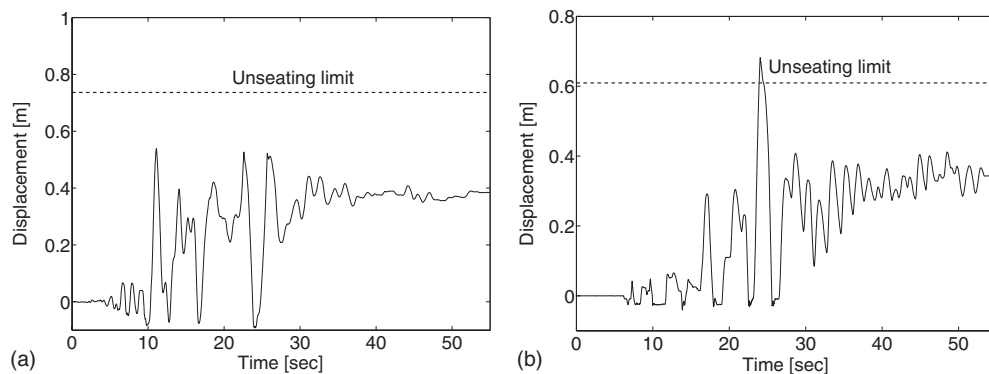

Figure 42. Relative horizontal displacement response histories between superstructure (girders) and abutment seat or pier at (a) left abutment, and (b) right interior expansion joint.
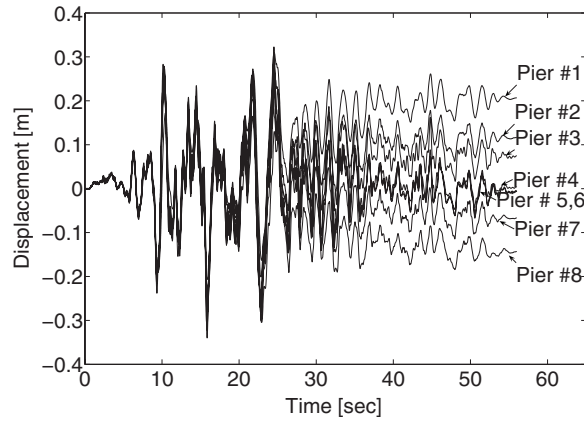
Figure 43. Total horizontal displacement response histories of all pier bases for Earthquake #2.

ment remains smaller than the unseating limit, while that between the superstructure and pier top at the right interior expansion joint exceeds the unseating limit at $t=23.91$ sec. Therefore, according to the present model and seismic response analysis, the 6th span of the HBMC Bridge would unseat at $t=23.91$ sec during Earthquake #2.

The total horizontal displacement response histories of the base of all bridge piers are shown in Figure 43 for Earthquake #2. It is observed that the base of each pier moves permanently towards the center of the river channel due to soil lateral spreading induced by reduction in soil shear strength caused by build-up of pore water pressure in cohesionless soil layers (mainly soil layers 5 and 7) during seismic response. The deformed FE mesh of the BFG system at the end of Earthquake #2 displayed in Figure 44 (with exaggerated scale) shows clearly that the approach embankments (together with the abutments) settle down significantly (0.41 m at the left abutment and 0.42 m at the right abutment) and move (0.20 m at the left abutment and 0.30 m at the right abutment) towards the center of the river channel together with the riverbanks, as indicated by the arrows in the figure. The plastic flow of the soil towards the center of the river channel
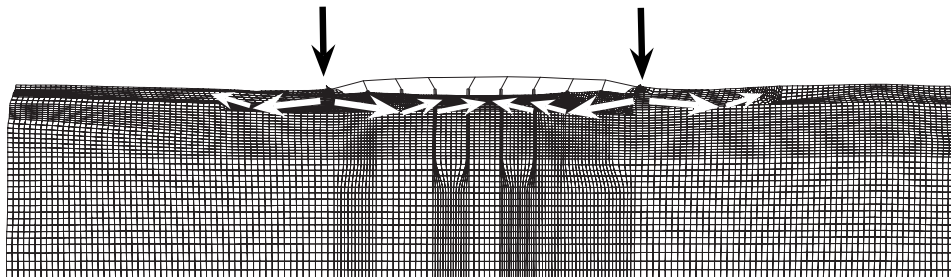

Figure 44. Deformed FE mesh at the end of Earthquake #2 (exaggerated scale).

elevates the river bed by about 0.05 m near the banks and 0.07 m at the center. Settlement and horizontal motion (towards the river center) of the approach embankments and abutments due to lateral soil spreading could affect significantly the post-earthquake bridge operability. Severe damage to bridges caused by similar pattern of lateral spreading has been observed in previous earthquakes (e.g., Kramer 1996, Figures 1.8 and 1.9). It is also observed from Figure 44 that plastic deformations of the foundation soil impose large residual plastic deformations and internal forces on the bridge structure. Animation of the seismic response of the BFG system shows clearly that the bridge structure and its foundations follow the low-frequency drifts of the soil due to its plastic flow towards the center of the river channel. Thus, according to the response simulation results obtained using the two-dimensional FE model presented here, the seismic response of the bridge in its longitudinal direction is mostly driven by the nonlinear inelastic response of the underlying soil. The seismic response mechanism of the HBMC Bridge shown here would be difficult to predict without explicit modeling of the local soil conditions, and inelastic behavior of the soil materials accounting for liquefaction effects.

CONCLUSIONS

A two-dimensional advanced nonlinear FE model was developed for an actual bridge, the Humboldt Bay Middle Channel (HBMC) Bridge near Eureka in northern California. The entire bridge-foundation-ground (BFG) system is considered in the model in order to investigate the effects of soil-foundation-structure interactions in the seismic response of the bridge. Realistic nonlinear constitutive models are used for the structural (concrete and reinforcing steel) and soil materials under cyclic loading conditions. The materials in the various soil layers are modeled using multi-yield-surface Von Mises and Drucker-Prager plasticity models incorporating liquefaction effects. A detailed mechanics-based model of the bridge piers is developed to account for the effects of lap splicing of the longitudinal reinforcement steel at the base of the piers. Lysmer-Kuhlemeyer absorbing boundaries are incorporated in the model of the BFG system so as to avoid spurious wave reflections along the boundaries of the computational soil domain. The model developed was used to perform small amplitude vibration analysis and earthquake response analysis of the BFG system. Based on the analysis results obtained, the following conclusions can be drawn:

(1) The model developed can provide detailed insights into the earthquake response of the nonlinear BFG system from the meso-scale (i.e., Gauss point, section fiber levels) to the macro-scale (e.g., overall soil lateral spreading mechanism). With explicit modeling of the underlying soil, this model can directly simulate the effects of the local site conditions, surface topography, hysteretic behavior (including liquefaction effects) of the soil materials, and soil-foundation-structure interaction in the seismic response analysis. These effects would be difficult, if not impossible, to simulate by modeling the underlying soil domain through equivalent nonlinear soil springs (e.g., p-y springs) and dashpots, as currently used in practice.

(2)   It was found that the response of the bridge structure is governed primarily by the nonlinear inelastic response of the underlying soil (i.e., inelastic site response) during earthquakes and that the plastic soil deformations impose large residual deformations and internal forces on the bridge structure after strong earthquakes. Effects of soil-foundation-structure interaction were observed mainly in the rocking at the base of the piers, with little SSI lateral effects.

(3)   The response of the bridge piers remains quasi-linear for earthquakes with a probability of exceedance of 50% in 50 years. This conclusion is also supported by other response simulations presented elsewhere (Zhang et al. 2006). However, the bridge shows significant vulnerabilities to earthquakes at the 2% in 50 years seismic hazard level. During such strong earthquakes, the analyses performed predict that the bridge piers would undergo extensive plastic deformations; the lap-spliced mechanism would be fully developed at the base of the piers with piers rocking on pile caps. Shear keys at the abutments and interior expansion joints would likely rupture, and as a result, unseating would also be likely to occur at these joints. Due to soil lateral spreading, the approach embankments and abutments would settle significantly and the underlying soil would "flow" plastically from each approach embankment to the back of the embankment and mainly to the center of the river channel. These predicted damage scenarios justify Caltrans' retrofit efforts described herein.

The modeling and analysis efforts presented here are integral parts of the ongoing development of a performance-based earthquake engineering (PBEE) methodology for bridge and building structures at the Pacific Earthquake Engineering Research (PEER) center. This methodology integrates probabilistic seismic hazard analysis, probabilistic seismic demand analysis, probabilistic seismic damage analysis, and probabilistic seismic loss analysis (Cornell and Krawinkler 2000). The HBMC Bridge modeled here serves as a bridge testbed in the development of this methodology. The model presented in this paper is used to predict probabilistically the seismic demand to be experienced by the HBMC Bridge at different seismic hazard levels, which is presented elsewhere (Zhang 2006).

It should be emphasized that the seismic analysis results presented in this study are based on a limited/restricted 2-D idealization of an actual 3-D bridge-foundation-ground system. However, it is expected that even with these limiting assumptions, the 2-D model presented is able to capture (at least qualitatively) the key features of the effects of SSI and soil lateral spreading on the seismic response of a BFG system with foundation soils vulnerable to liquefaction. This study provides a first step towards the development of more realistic and more accurate 3-D models.

Finally, it is worth mentioning that a number of factors such as ground motion spatial variability (wave passage and incoherency effects), spatial variation of soil dynamic properties within soil layers, and uncertainties in soil dynamic properties, which may affect the results of the present study, have not been considered.

ACKNOWLEDGMENTS

REFERENCES

Acero, G., 2005. Seismic Response of Columns with Unconfined Lap-Splices, M.S. thesis, University of California at San Diego, CA.

Arulmoli, K., Muraleetharan, K. K., Hossain, M. M., and Fruth, L. S., 1992. *VELACS: Verification of liquefaction analyses by centrifuge studies, laboratory testing program, soil data report*, Project No. 90-0562, *The Earth Technology Corporation*, Irvine, California.

Ayala, G. A., and Aranda, G. R., 1977. Boundary conditions in soil amplification studies, in *Proceedings of the 6th World Conference on Earthquake Engineering*, Vol. 6, New Dehli, India.

Bielak, J., 1978. Dynamic response of nonlinear building-foundation systems, *Earthquake Eng. Struct. Dyn.* **6**, 17–30.

Caltrans, 2000. Memorandum, Humboldt Bay Middle Channel Bridge, File 01-Hum-255-0.7, *Engineering Service Center, Division of Structural Foundation -MS 5*, California Department of Transportation.

——, 2002. Humboldt Bay bridges seismic substructure retrofit, http://www.dot.ca.gov/dist1/d1projects/humbaybridges, November 29, 2005.

Ciampoli, M., and Pinto, P., 1995. Effects of soil-structure interaction on inelastic seismic response of bridge piers, *J. Struct. Eng.* **121**, 806–814.

Clough, R., and Penzien, J., 2003. *Dynamics of Structures*, 2nd edition, Computers and Structures Inc., Berkeley, California.

Cornell, C. A., and Krawinkler, H., 2000. Progress and challenges in seismic performance assessment, *PEER Center News*, Vol. 3, No. 2, Spring 2000.

Dendrou, B., Werner, S., and Toridis, T., 1985. Three-dimensional response of a concrete bridge system to traveling seismic waves, *Comput. Struct.* **20**, 593–603.

Dobry, R., Taboada, V., and Liu, L., 1995. Centrifuge modeling of liquefaction effects during earthquakes, Keynote Lecture, *Proceedings of the 1st International Conference on Earthquake Geotechnical Engineering* (IS-Tokyo), Ishihara, K., (editor), vol. 3, Balkema, Netherlands, 1291–1324.

Dominguez, N. D., and Soler, P. A., 1999. *GID User Manual*, International Center for Numerical Methods in Engineering, Barcelona, Spain.

Duncan, J., Horz, R., and Yang, T., 1989. Shear strength correlations for geotechnical engineering, Report, Department of Civil Engineering, Virginia Tech.

Elgamal, A., Lai, T., Yang, Z., and He, L., 2001. Dynamic soil properties, seismic downhole arrays and applications in practice (CD-ROM), State-of-the-art paper, in *Proceedings of the 4th International Conference. on Recent Advances in Geotechnical Earthquake Engineering and Soil Dynamics*, S. Prakash (editor), San Diego, California, March 26–31.

Elgamal, A., Yang, Z., Parra, E., and Ragheb, A., 2003. Modeling of cyclic mobility in saturated cohesionless soils, *Int. J. Plast.* **19**, 883–905.

Eyre, R., and Tilly, G. P., 1977. *Damping measurements on steel and composite bridges*, in *Symposium on Dynamic Behavior of Bridges, Supplementary Report 275*, Transport and Road Research Laboratory, Crowthorne, UK.

Geomatrix Consultants, 1994. Seismic ground motion study for Humboldt Bay bridges on Route 225, Humboldt County, California, Contract No. 59N772. Report prepared for Caltrans Division of Structures.

Goel, R. K., 1997. Earthquake characteristics of bridges with integral abutments, *J. Struct. Eng.* **123**, 1435–1443.

Goel, R. K., and Chopra, A. K., 1997. Evaluation of bridge abutment capacity and stiffness during earthquakes, *Earthquake Spectra* **13**, 1–21.

Idriss, I. M., 1990. Response of soft soil sites during earthquakes, in *Proceedings, H. Bolton Seed Memorial Symposium*, J. M. Duncan (editor), vol. 2, BiTech Publishers, Vancouver, British Columbia, 273–289.

Idriss, I. M., and Sun, J. I., 1993. User's Manual for SHAKE91: A computer program for conducting equivalent linear seismic response analyses of horizontally layered soil deposits. Center for geotechnical modeling, University of California, Davis, California.

Jeremic, B., Kunnath, S., and Xiong, F., 2004. Influence of soil-foundation-structure interaction on seismic response of the I-880 viaduct, *Eng. Struct.* **263**, 391–402.

Joyner, W. B., 1975. Method for calculating nonlinear seismic response in 2-dimensions, *Bull. Seismol. Soc. Am.* **65**, 1337–1357.

Kammerer, A., Wu, J., Pestana, J., Riemer, M., and Seed, R., 2000. *Cyclic simple shear testing of Nevada sand for PEER Center project 2051999*, *Research Report No. UCB/GT/00–02*, University of California at Berkeley, California.

Kappos, A. J., Manolis, G. D., and Moschonas, I. F., 2002. Seismic assessment and design of R/C bridges with irregular configuration, including SSI effects, *Eng. Struct.* **24**, 1337–1348.

Kent, D. C., and Park, R., 1971. Flexural members with confined concrete, *J. Struct. Div.* **97**, 1969–1990.

Kramer, S. L., 1996. *Geotechnical Earthquake Engineering*, Prentice Hall, Upper Saddle River, NJ, 653 pp.

Liu, A., Stewart, J., Abrahamson, N., and Moriwaki, Y., 2001. Equivalent number of uniform stress cycles for soil liquefaction analysis, *J. Geotech. Geoenviron. Eng.* **127**, 1017–1026.

Luco, J. E., and Hadjian, A. H., 1974. Two-dimensional approximations to the three-dimensional soil-structure interaction problem, *Nucl. Eng. Des.* **31**, 195–203.

Lysmer, J., and Kuhlemeyer, R. L., 1969. Finite dynamic model for infinite media, *J. Engrg. Mech. Div.* **95**, 859–877.

McCallen, D. B., and Romstad, K. M., 1994. Analysis of a skewed short-span, box-girder overpass, *Earthquake Spectra* **10**, 729–755.

McKenna, F., and Fenves, G. L., 2001. The OpenSees command language manual, version 1.2, http://opensees.berkeley.edu, Pacific Earthquake Engineering Research Center, University of California, Berkeley.

Meyerhof, G. G., 1956. Penetration tests and bearing capacity of cohesionless soils, *J. Soil Mech. and Found. Div.* **82**(SM1), 1–19.

Mitchell, J., and Katti, R., 1981. Soil improvement state-of-the-art report, General Reports, in *Proceedings of 10th International Conference of Soil Mechanics and Foundation Engineering*, vol. 4, Stockholm, 264–320.

Mylonakis, G., and Gazetas, G., 2000. Seismic soil-structure interaction: beneficial or detrimental? *J. Earthquake Eng.* **4**, 277–301.

Mylonakis, G., Nikolaou, A., and Gazetas, G., 1997. Soil-pile-bridge seismic interaction: kinematic and inertial effects. Part I: soft soil, *Earthquake Eng. Struct. Dyn.* **26**, 337–359.

Porter, K. A., 2003. An overview of PEER's performance-based earthquake engineering methodology, in *Proceedings of the 9th International Conference on Applications of Statistics and Probability in Civil Engineering*, San Francisco, California, July 6–9.

Prevost, J. H., 1985. A simple plasticity theory for frictional cohesionless soils, *Soil Dyn. Earthquake Eng.* **4**, 9–17.

Seed, H. B., Ugas, C., and Lysmer, J., 1976. Site-dependent spectra for earthquake-resistant design, *Bull. Seismol. Soc. Am.* **66**, 221–243.

Seed, H. B., Wong, R. T., Idriss, I. M., and Tokimatsu, K., 1984. *Moduli and damping factors for dynamic analysis of cohesionless soils*, *Report UCB/EERC-84/14*, *Earthquake Engineering Research Center*, University of California, Berkeley, California.

Seed, R., Cetin, K., Moss, R., Kammerer, A., Wu, J., Pestana, J., Riemer, M., Sancio, R., Bray, J., Kayen, R., and Faris, A., 2003. Recent advances in soil liquefaction engineering: a unified and consistent framework, Keynote Presentation, *26th Annual ASCE Los Angeles Geotechnical Spring Seminar*, H.M.S. Queen Mary, Long Beach, CA.

Silva, P. F., and Seible, F., 2001. Seismic performance evaluation of CISS piles, *ACI Struct. J.* **98**, 36–49.

Silva, W., 2003. *Soil response to earthquake ground motion*, *Research Project RP2556-07 Final Report*, Woodward-Clyde Consultants, Walnut Creek, CA.

Somerville, P., and Collins, N., 2002. Ground motion time histories for the Humboldt Bay Bridge, *Report of the PEER Performance Based Earthquake Engineering Methodology Testbed Program*, Pacific Earthquake Engineering Research Center, University of California at Berkeley, Berkeley, California.

Spacone, E., Filippou, F. C., and Taucer, F. F., 1996. Fibre beam-column model for non-linear analysis of R/C frames: Part I. Formulation, *Earthquake Eng. Struct. Dyn.* **25**, 711–725.

Spyrakos, C., 1992. Seismic behavior of bridge piers including soil-structure interaction, *Comput. Struct.* **43**, 373–384.

Trochanis, A. M., Bielak, J., and Christiano, P., 1991. Three-dimensional nonlinear study of piles, *J. Geotech. Engrg.* **117**, 429–447.

Werner, S. D., Beck, J. L., and Levine, M. B., 1987. Seismic refraction evaluation of Meloland road overpass using the 1979 Imperial Valley earthquake records, *Earthquake Eng. Struct. Dyn.* **15**, 249–274.

Werner, S. D., Beck, J. L., and Nisar, A., 1990. Dynamic tests and seismic excitation of a bridge structure, *Proceedings of 4th U.S. National Conference on Earthquake Engineering*, 1, 1037–1046.

Werner, S. D., Crouse, D. B., Katafygiotis, L. S., and Beck, J. L., 1994. Use of strong motion records for model evaluation and seismic analysis of a bridge structure, in *Proceedings of the 5th U.S. National Conference on Earthquake Engineering*, Vol. 1, 511–520.

Wilson, J. C., and Tan, B. S., 1990a. Bridge abutments: formulation of simple model for earthquake response analysis, *J. Eng. Mech.* **116**, 1828–1837.

——, 1990b. Bridge abutments: assessing their influence on earthquake response of Meloland road overpass, *J. Eng. Mech.* **116**, 1838–1856.

Yang, Z., Elgamal, A., and Parra, E., 2003. Computational model for cyclic mobility and associated shear deformation, *J. Geotech. Geoenviron. Eng.* **129**, 1119–1127.

Yang, Z., Lu, J., and Elgamal, A., 2005. OpenSees geotechnical capabilities developed at U.C. San Diego. User Manual, http://cyclic.ucsd.edu/opensees, November 29.

Youd, T. et al., 2001. Liquefaction resistance of soils: summary report from the 1996 NCEER and 1998 NCEER/NSF workshops on evaluation of liquefaction resistance of soils, *J. Geotech. Geoenviron. Eng.* **127**, 817–833.

Zhang, J., and Makris, N., 2002. Seismic response analysis of highway overcrossings including soil-structure interaction, *Earthquake Eng. Struct. Dyn.* **31**, 1967–1991.

Zhang, Y., Yang, Z., Bielak, J., Conte, J. P., and Elgamal, A., 2003. Treatment of seismic input and boundary conditions in nonlinear seismic analysis of a bridge ground system, in *Proceedings of the 16th ASCE Engineering Mechanics Conference*, University of Washington, Seattle, July 16–18.

Zhang, Y., 2006. Probabilistic Structural Seismic Performance Assessment Methodology and Application to an Actual Bridge-Foundation-Ground System, Ph.D. thesis, University of California at San Diego, CA.